



Electrospun poly-(L-lactide) scaffold enriched with GO-AuNPs nanocomposite stimulates skin tissue reconstruction *via* enhanced cell adhesion and controlled growth factors release

Michał Pruchniewski^a, Barbara Strojny-Cieślak^{a,*}, Paweł Nakielski^b, Katarzyna Zawadzka^a, Kaja Urbańska^c, Daniel Rybak^b, Anna Zakrzewska^b, Marta Grodzik^a, Ewa Sawosz^a

^a Department of Nanobiotechnology, Institute of Biology, Warsaw University of Life Sciences, Warsaw 02-777 Poland

^b Department of Biosystems and Soft Matter, Institute of Fundamental Technological Research, Polish Academy of Sciences, Warsaw 02-106 Poland

^c Department of Morphological Sciences, Institute of Veterinary Medicine, Warsaw University of Life Sciences, Warsaw 02-777 Poland

ARTICLE INFO

Keywords:

Wound healing
Electrospun fibers
Graphene oxide
Gold nanoparticles
Proregenerative cell scaffold

ABSTRACT

The disruption of homeostasis in the tissue microenvironment following skin injury necessitates the provision of a supportive niche for cells to facilitate the restoration of functional tissue. A meticulously engineered cell-scaffold biointerface is essential for eliciting the desired cellular responses that underpin therapeutic efficacy. To address this, we fabricated an electrospun poly-(L-lactide) (PLLA) cell scaffold enriched with graphene oxide (GO) and gold nanoparticles (AuNPs). Comprehensive characterization assessed the scaffolds' microstructural, elemental, thermal, and mechanical properties. *In vitro* investigations evaluated the biocompatibility, adhesive and regenerative capabilities of the scaffolds utilizing human keratinocytes (HEKa), fibroblasts (HFFF2), and reconstructed epidermis (EpiDerm™) models. The results demonstrated that the incorporation of the GO-Au composite substantially altered the nanotopography and mechanical properties of the PLLA fibers. Cells effectively colonized the PLLA + GO-Au scaffold while preserving their structural morphology. Furthermore, PLLA + GO-Au treatment resulted in increased epidermal thickness and reduced tissue porosity. The scaffold exerted a significant influence on actin cytoskeleton architecture, facilitating cell adhesion through the upregulation of integrins, E-cadherin, and β -catenin. Keratinocytes exhibited enhanced secretion of growth factors (AREG, bFGF, EGF, EGF R), while fibroblast secretion remained stable. These findings endorse the scaffold's potential for regulating cellular fate and preventing hypertrophic tissue formation in skin tissue engineering.

1. Introduction

The tissue engineering triad represents a fundamental concept within the field of regenerative medicine, serving as a sophisticated alternative to traditional therapeutic strategies [1,2]. This triad comprises three integral components: cell populations, which serve as the primary therapeutic agents; a biomimetic scaffold that provides structural support and spatial organization for cellular proliferation and differentiation; and bioactive molecules that modulate cellular behavior and enhance the regenerative response [3]. Skin wound healing is a highly orchestrated biological process that necessitates collaborative interaction among diverse cellular populations, aimed at reestablishing both the architectural integrity and functional capability of the tissue.

Following skin injury, the structural integrity of the extracellular matrix (ECM) is compromised, leading to alterations in the tissue microenvironment that impede the efficacy of cellular activities vital for regeneration [4]. The loss of ECM components not only disrupts cell-matrix interactions but also creates an unfavorable niche for the recruitment, proliferation, and differentiation of endogenous cells, ultimately impairing the wound-healing cascade [5–7]. Thus, the incorporation of patient-derived cells, expanded *in vitro* and subsequently embedded within a biomimetic scaffold that elicits a biological response through the inclusion of bioactive substances, can activate endogenous cellular activity. It is essential to modulate cellular stimulation, as unregulated stimulation may result in the formation of hypertrophic tissues. These tissues are distinguished by an abnormal proliferation of fibroblasts,

* Corresponding author.

E-mail address: barbara_strojny-cieslak@sggw.edu.pl (B. Strojny-Cieślak).

<https://doi.org/10.1016/j.matdes.2025.113713>

Received 10 October 2024; Received in revised form 6 January 2025; Accepted 10 February 2025

Available online 11 February 2025

0264-1275/© 2025 The Authors. Published by Elsevier Ltd. This is an open access article under the CC BY license (<http://creativecommons.org/licenses/by/4.0/>).

leading to the development of non-functional tissue with compromised physiological properties [8].

Electrospinning is a technique that facilitates the production of porous scaffolds for cells, exhibiting structural properties analogous to the ECM, while simultaneously enabling the modulation of polymer fiber topography at the nanometer scale [9,10]. Cells are able to mechanically detect even subtle variations in the growth surface, which, in turn, initiates a cascade of molecular events regulated by surface characteristics [11].

Poly-(L-lactide) (PLLA) is a widely utilized aliphatic polyester in the field of electrospinning, owing to its advantageous characteristics, which encompass biocompatibility, biodegradability, and favorable processability [12–14]. PLLA-based scaffolds provide a substrate for cellular adhesion, with their architectural configurations affecting critical cellular behaviors such as adhesion [15,16], migration [17,18] and vascularization process [19]. The inherent modifiability of electrospun PLLA facilitates the incorporation of bioactive agents into the nonwoven fiber matrix, thereby enhancing the biological efficacy of the polymer. While PLLA can independently function as a scaffold to support cell growth, the application of surface coatings or the nanostructuring of fibers with bioactive compounds can further increase its functional capabilities. Graphene oxide (GO) and gold nanoparticles (Au NPs) represent significant nanostructuring agents for electrospun PLLA fibers. GO not only influences the nanotopography of polymeric fibers and enhances cellular adhesion [20–22] but also acts as an effective substrate for the deposition of metallic NPs, thereby reducing their cytotoxicity [23]. Au NPs serve a multifaceted role in skin regeneration through various mechanisms, including the enhancement of cellular proliferation [24], regulation of inflammatory responses [25] and protection against oxidative stress [26]. The incorporation of even a modest quantity of these nanostructures can markedly influence the physicochemical properties of the scaffold, while also exerting a favorable impact on cellular responses by facilitating regenerative processes.

The distinctive characteristics of PLLA cell scaffolds incorporated with GO and Au NPs may stem not only from their biomimetic architecture but also from the ability to meticulously modulate the overall properties of the polymeric fibers. The integration of GO and Au NPs into biomaterials significantly alters nanoscale interactions, leading to modifications in the mechanosensing mechanisms of cells and consequently influencing their biological responses. [27–31]. Moreover, the synergistic effects between GO and Au NPs [32–35] position these nanocomposites as promising candidates for the modulation of cellular responses to biomolecular factors derived from animal sources, which may otherwise pose adverse effects. Although prior investigations have examined the roles of GO and Au NPs across various biomaterials and nanosystems, there remains a paucity of understanding regarding their synergistic interactions within PLLA scaffolds, particularly in the context of molecular responses and mechanotransduction. This existing knowledge gap underscores the need for further inquiry into the effective integration of these materials to regulate cellular activity at the molecular level.

In the present study, we investigated the impact of incorporating GO-Au into the electrospun PLLA fibers on the modifications of its physicochemical properties, as well as the resultant biological effects induced by this modification, including original findings on biomaterial selectivity toward keratinocytes stimulation along with the fibroblasts unresponsiveness in the context of growth factors release. We systematically analyzed the mechanistic relationships between the biomaterial and various cell models *in vitro*, including a tissue model representing the epidermis, to elucidate the influence of fibers nanotopography at the subcellular and molecular levels. This analysis focused on assessing the materials' cell-adhesive characteristics and proregenerative properties, thereby shedding light on the underlying mechanisms that govern these associations.

2. Experimental

2.1. Fabrication of cell scaffold

2.1.1. Preparation of electrospinning solution

The composite solution was prepared by combining graphene oxide (GO; Advanced Graphene Products, Poland) with gold nanoparticles (Au NPs; Nano-Tech, Poland) in a mass ratio of 5:1, accordingly to our previously published paper [22]. Prior to the combination, the individual nanostructures were subjected to sonication in a Cell™ Ultrasonic Liquid Processor (Sonics&Materials, USA) for 5 min at 500 W. The solutions were mixed and sonicated again to ensure thorough deposition of Au NPs onto the surface of GO by self-assembly. The resulting GO-Au nanocomposite solution was dried at a temperature of 40°C and subsequently suspended in N,N-dimethylformamide (DMF; POCh, Poland) via a 1-hour stirring process, followed by a 30-minute sonication. Our previous findings, supported by scanning electron microscopy (SEM) visualization, indicated that the size of GO-Au was approximately 4 µm, while dynamic light scattering (DLS) analysis revealed a hydrodynamic diameter of about 300 nm [22].

Poly-(L-lactide) (PLLA; PL18, Corbion Purac, Netherlands) was separately dissolved in chloroform (CHCl₃; POCh, Poland) by stirring overnight at room temperature. After the individual components were completely dissolved, the PLLA/CHCl₃ solution was added to the GO-Au/DMF solution, and the mixture was stirred for an additional hour. The concentration of PLLA relative to the solvents mixture was maintained at 6.75% (w/w), while the concentration of GO-Au relative to PLLA was set at 0.1% (w/w). The CHCl₃:DMF ratio was kept constant at 9:1 (w/w). The comprehensive characterization of GO-Au, which has been previously reported in our publication [22], served as the foundation for the choice of Au NPs as the metallic nanoparticle component and the optimal GO:Au ratio.

2.1.2. Electrospinning

Cell scaffolds were fabricated using an electrospinning technique. A 1 mL syringe coupled with a 24G steel needle was utilized to extrude the polymer solution at a controlled flow rate of 0.8 mL/h. Two glass slides with an area of 25 mm × 75 mm, serving as grounded collectors, were positioned at a distance of 15 cm from the needle. Electrospinning was conducted under ambient conditions (room temperature and humidity range of 40–55%) for a period of 45 min at a positive voltage of 17 kV. Prior to *in vitro* testing, biomaterials were sterilized in 70% ethanol for 30 min, followed by double rinsing with ultrapure water for 30 min and subsequent drying.

2.2. Biomaterial characterization

2.2.1. Morphological characterization

To assess the morphology of the electrospun mats, the samples were initially sputtered with a thin layer of gold (about 8 nm thick) using an SC7620 Polaron mini sputter coater (Quorum Technologies Ltd, UK). Visualization was performed using field emission scanning electron microscopy Nova NanoSEM 450 (FE-SEM; FEI Company, USA) at accelerating voltage of 5 kV. The fiber diameter distribution as well as the orientation of the fibers were assessed using ImageJ software (National Institutes of Health, USA).

2.2.2. Physical-chemical characterization

The technique of attenuated total reflection-Fourier infrared spectroscopy (ATR/FT-IR) was used to detect chemical bonds of the tested materials. Infrared spectra were recorded using a Vertex70 FT-IR spectrometer (Bruker, USA) in the wavenumber range of 400–4000 cm⁻¹ with a resolution of 2 cm⁻¹ (12 scans per sample).

Thermal properties of materials were analyzed by TGA/DSC (thermogravimetric analysis/differential scanning calorimetry) on a TA STD Q600 thermogravimetric device (TA Instruments, USA). Measurements

were performed under argon flow for approximately 10 mg of sample placed in a corundum crucible heated to 650°C at a heating rate of 10°C/min.

A X-ray photoelectron spectroscopy (XPS) analysis was performed to investigate the elemental composition of the surface of cell scaffolds. The measurements were conducted using an XPS/AES Microlab 350 spectrometer (Thermo Electron, USA) equipped with a non-monochromatic Al K α X-ray source operating at an energy of 1486.6 eV and a power of 300 W. The XPS spectra were recorded with a horizontal resolution of 0.2 cm² at a depth of 10 nm in the energy range from 1350 eV to 0 eV, using an energy step size of 1.0 eV for survey spectra and 0.1 eV for high-resolution spectra. The recorded high-resolution XPS spectra were deconvoluted using Thermo Advantage software (version 5.41; Thermo Fisher Scientific, USA).

Mechanical properties of the materials were evaluated through tensile testing using a CTX texture analyzer (AMETEK Brookfield, USA). Specimens were cut into rectangular strips with dimensions of 1 cm \times 4 cm. For each material, the analysis was performed in three repetitions. The samples were subjected to uniaxial tension at a constant strain rate of 0.5 mm/min. The resulting stress–strain curves were used to determine Young's modulus, tensile modulus, and elongation at break. The results were normalized to the thickness of the samples measured using Kroepelin flat calipers.

The measurement of the contact angle (CA) to assess the hydrophilic properties of the scaffolds was conducted using an OCA15 goniometer (Data Physics Instruments GmbH, Filderstadt, Germany). The sessile drop method was employed, in which a 1 μ L droplet of deionized water was applied to the biomaterials. Three measurements were taken for each sample at room temperature.

2.3. Biological models

2.3.1. Cell lines

Human primary epidermal keratinocytes (HEKa) and human fetal foreskin fibroblasts (HFFF2) were obtained from the American Type Culture Collection (ATCC, USA) and Sigma-Aldrich (USA), respectively. HEKa cells were cultured in Keratinocyte Growth Medium 2 supplemented with 0.004 mL/mL bovine pituitary extract, 0.125 ng/mL epidermal growth factor, 5 μ g/mL insulin, 0.33 μ g/mL hydrocortisone, 0.39 μ g/mL epinephrin, 10 μ g/mL transferrin, and 0.06 mM CaCl₂ (Promocell, Germany). HFFF2 cells were cultured in Dulbecco's Modified Eagle's Medium (DMEM; Gibco, USA) containing 1 g/L glucose and GlutaMAX supplemented with 10% fetal bovine serum (FBS; Gibco). To prevent microbial contamination, 1% Antibiotic-Antimycotic Solution (Sigma-Aldrich) was added to the medium. The culture medium was refreshed every 2 days.

Cells were maintained under standard conditions of 37°C, 5% CO₂, and 95% relative humidity. The HEKa cells were subcultured at a maximum of 8 passages, while the HFFF2 cells were subcultured at a maximum of 10 passages, to maintain their viability and original features.

2.3.2. Tissue model

Reconstructed human epidermal tissue (EpiDerm™; EPI-200) was purchased from MatTek Corporation (USA). A three-dimensional model was derived from normal human-derived epidermal keratinocytes (NHEK) and layered in a stratified manner (from top to bottom): stratum corneum, granular, spinous, and basal layers. Tissues were maintained on an insert with a porous membrane bottom on an air–liquid interface in EPI-100-NMM medium under standard conditions.

2.3.3. Experimental conditions

To assess the biological activity of the scaffold, a direct method was used, which involved seeding cells on the biomaterial. Silicone inserts have been applied on the biomaterial ensuring a controlled and repeatable environment for cells, allowing for cell growth and

attachment to a precisely defined surface. Cells were seeded in 2-well inserts (Ibidi GmbH, Germany) with a surface area of 0.22 cm²/well or 8-well flexiPERM® inserts (Sarstedt, Germany) with a surface area of 0.9 cm²/well. As control surfaces, tissue culture plastic (TCP) or glass coverslips (confocal microscopy) were used. The incubation times varied depending on the specific analysis and will be reported in the subsequent methodology sections.

Tissues, upon receipt, were immediately conditioned to facilitate optimal adaptation. Tissue inserts, freed from agarose residue, were positioned in 6-well plates containing 0.9 mL of growth medium and incubated for 1 h under standard conditions. Subsequently, they were transferred to fresh medium and further incubated overnight. Four experimental groups were established, each with triplicates: (1) the negative control (NC) treated with 100 μ L Phosphate-Buffered Saline (PBS; Gibco); (2) the PLLA-treated group; (3) the PLLA+GO-Au-treated group; and (4) the positive control (PC) maintained in PBS throughout the experiment and incubated with 5% sodium dodecyl sulfate (SDS; Sigma-Aldrich) at 37°C for 10 min to induce tissue damage at the end of the experiment. Sterile biomaterial discs with a diameter matching the tissue were directly applied to the biomaterial-treated tissue samples. The treatment of tissues was conducted for 72 h. The culture medium was refreshed every 24 h, collected and stored at –80°C for further analysis.

2.4. Cellular biocompatibility

2.4.1. XTT mitochondrial activity assay

Cell viability was assessed via the measurement of mitochondrial activity, utilizing the XTT reagent (2,3-bis-(2-methoxy-4-nitro-5-sulphophenyl)-2H-tetrazolium-5-carboxanilide), which is converted into the orange formazan product through the action of succinate reductase, an enzyme characteristic of metabolically active cells.

Cells were directly plated onto TCP or biomaterials in 2-well inserts at a density of 1.5×10^4 cells per well. Following incubation for either 24 h or 72 h, 40 μ L of culture medium was removed from each well and replaced with 40 μ L of the working solution (electron coupling reagent and XTT labeling reagent in a ratio of 1:6) from the CyQUANT XTT Cell Viability Assay kit (Invitrogen, USA). The cells were then incubated for an 1 h at 37°C. After incubation, the medium was transferred to a clean 96-well plate. Subsequently, absorbance measurements were conducted using an Infinite®200 PRO microplate reader with i-control™ software (Tecan Group Ltd, Germany) at wavelengths of 450 nm and 660 nm. The results are presented as the mean percentage ($n = 5$) for each experimental group relative to the mean control value (100%), with blank values subtracted.

2.4.2. LDH leakage assay

To investigate the influence of biomaterials on the integrity of the cell membrane, a lactate dehydrogenase (LDH) release assay was conducted. LDH is a cellular enzyme that serves as a marker for cytotoxic effects, as its release into the extracellular compartment is indicative of cell damage caused by the studied factor. The assay relies on LDH-catalyzed reactions, reducing NAD⁺ to NADH/H⁺ and forming red formazan.

Cells were seeded directly onto TCP or biomaterial in 2-well inserts at a density of 1.5×10^4 cells per well and incubated for 24 or 72 h. The cells were seeded in serum-reduced medium in order to avoid the influence of FBS on the test results. To determine maximum LDH release, a positive control (PC) was prepared by dissolving cells cultured on TCP in 1% Triton X-100 (Sigma-Aldrich) for 30 min at 37°C. Then, 75 μ L of medium was transferred to a 96-well plate and centrifuged at 1200 RPM for 5 min. Subsequently, 50 μ L of supernatant was transferred to a 96-well plate and mixed with 50 μ L of reaction buffer provided in the Cytotoxicity Detection Kit (LDH; Roche, Germany). The plate was incubated in the dark on an orbital shaker for 30 min, followed by measurement of absorbance at a wavelength of 490 nm and reference

wavelength of 680 nm using an Infinite®200 PRO microplate reader. The results are presented as the mean percentage ($n = 5$) of cytotoxicity according to the formula:

$$\% \text{ of cytotoxicity} = \frac{(\text{exp. value} - \text{low control})}{(\text{high control} - \text{low control})} \times 100\%$$

where exp. value is the absorbance for each test group, low control is the average absorbance for the negative control cells, high control is the average absorbance for the cells of the positive group. Blanks were included in the calculations.

2.4.3. Visualization of cells

The morphology of cells and cell colonization on biomaterials were visualized using a scanning electron microscope JEOL JSM-6390LV (JEOL Ltd., Japan). 1.5×10^4 cells were seeded into a 2-well insert placed on the biomaterial. After 24h or 72h of incubation, the cells were rinsed three times with a warmed $\text{PBS}^{\text{Ca}^{2+}/\text{Mg}^{2+}}$ and fixed in 2.5% glutaraldehyde (GA; Sigma-Aldrich) at 4°C overnight. Subsequently, the cells were rinsed three times with cold phosphate buffer (PB) and post-fixed in 1% osmium tetroxide for 45 min at room temperature. After a further three rinses with PB, the cells were dehydrated using an ethanol gradient: 25%, 50%, 60%, 70%, 80%, 90%, and 95% (5 min for each concentration), followed by a final rinse with 100% ethanol (3×15 min). The samples were then air-dried for over 24 h. A thin layer of gold was applied to the samples by gold sputtering and visualization was performed using FE-SEM at an accelerating voltage of 5 kV.

Visualization of the actin cytoskeleton architecture was performed after 24 h of incubation. Cells were washed with warm $\text{PBS}^{\text{Ca}^{2+}/\text{Mg}^{2+}}$ and fixed in 4% paraformaldehyde (PFA; Sigma Aldrich) for 15 min at room temperature. Then, cells were washed three times with $\text{PBS}^{-/}$ and labeled with 300 μM 4',6-diamidino-2-phenylindole (DAPI; nuclear labeling) and 6.6 μM phalloidin conjugated with Alexa Fluor 633 (actin cytoskeleton labeling) diluted in $\text{PBS}^{-/}$, both purchased from Molecular Probes (USA). After 30 min of incubation in the dark, slides were washed three times with $\text{PBS}^{-/}$, twice with distilled water, and mounted with Fluoromount Aqueous Mounting Medium (Sigma Aldrich). Visualization was performed using FV-100 confocal microscope (Olympus, Japan).

2.5. Tissue biocompatibility

2.5.1. LDH leakage assay

In order to determine the potential toxic effect of the biomaterial on EpiDerm™ tissues, an LDH leakage assay was performed. The culture medium was refreshed 24h, 48h, and 72h after the start of the experiment. Post-incubation media were snap-frozen in liquid nitrogen and stored at -80°C , thus preventing LDH degradation. The media was thawed and centrifuged (1200 RPM, 10 min) directly before further analysis. 50 μL of medium was applied onto 96-well plate in duplicate for each tissue. Next, 50 μL of reaction buffer (Roche) was added and remaining steps were performed as in section 2.4.2. Results are presented as mean percentage ($n = 6$) of negative control at a given time point.

2.5.2. Histological examination

Tissue morphology was assessed using hematoxylin and eosin (HE) histological staining. EpiDerm™ skin samples after 72 h of treatment were thoroughly washed with $\text{PBS}^{-/}$, then fixed in buffered formaldehyde (pH 7.2; Sigma-Aldrich) overnight at 4°C. Subsequently, the tissues were dehydrated in an ascending ethanol gradient. The tissues were embedded in paraffin (Paraplast, Sigma-Aldrich) and sectioned at a thickness of 5 μm using a microtome (Leica, Germany). Finally, routine HE staining was performed and visualized using a light microscope DM750 (Leica). Morphometric analysis, based on which the thickness of the stratum corneum and stratum germinativum, as well as the porosity of the stratum corneum, was determined using ImageJ software.

2.5.3. Hemolysis assay

The hemolysis assay was performed to evaluate the hemolytic activity of scaffolds. Blood samples were obtained from three distinct donors, and all procedures involving blood collection were performed in accordance with the Declaration of Helsinki. Detailed methodology of the experiment is provided in the Supplementary Materials.

2.6. Adhesion assessment

2.6.1. Adhesion kinetics

To investigate the adhesion kinetics, cells were directly seeded onto either glass slide or a biomaterial surface in the 2-well insert, with a seeding density of 2.5×10^4 cells per well. Cells were incubated for 60, 120, 240, and 480 min, after which they were washed three times with warm $\text{PBS}^{\text{Mg}^{2+}/\text{Ca}^{2+}}$ to remove non-adherent cells. Following fixation in 4% paraformaldehyde for 15 min, cell nuclei were labeled with 300 μM DAPI for 15 min in the dark. The slides were then washed three times with $\text{PBS}^{-/}$, twice with distilled water, and mounted in Fluoromount Aqueous Mounting Medium. Visualization was performed using a FV-100 confocal microscope. The results were expressed as the number of cell nuclei per square millimeter ($n = 6$). Cell nuclei counting analysis was performed using FIJI software.

2.6.2. Cell adhesion molecules expression analysis

The expression of selected cell adhesion molecules (CAMs) was investigated at the mRNA level via real-time quantitative polymerase chain reaction (PCR) analysis. The following genes were analyzed: $\alpha 2$ integrin (*INGa2*), $\alpha 3$ integrin (*INGa3*), $\alpha 4$ integrin (*INGa4*), $\alpha 5$ integrin (*INGa5*), $\alpha 6$ integrin (*INGa6*), $\beta 1$ integrin (*INGβ1*), *E-cadherin*, β -catenin, *focal adhesion kinase (FAK)*.

Cells were seeded directly onto TCP or biomaterial surfaces in 8-well inserts at a density of 1×10^5 cells per well. Following a 24-hour incubation period, the cells were washed with $\text{PBS}^{-/}$ and subsequently dissociated using TrypLE™ Express Enzyme (Gibco). The enzyme activity was neutralized by addition of 10% FBS in $\text{PBS}^{-/}$, and the cell suspension was centrifuged at 1200 RPM for 5 min. The cell pellets were then washed twice with $\text{PBS}^{-/}$. Cells were collected from three independent pieces of biomaterial.

The ROTI®Prep RNA kit (Carl Roth GmbH, Germany) was used to isolate total RNA. Cell pellet was lysed in Lysis Buffer LSR included in the kit, and the remaining steps were performed according to the manufacturer's instructions. Elution was performed in 30 μL RNase-free water. RNA concentration and quality were measured using NanoDrop 2000 (Thermo Fisher Scientific). Equalized samples were stored at -80°C for further analysis.

Reverse transcriptase polymerase chain reaction (RT-PCR) was conducted using the cDNA High Capacity Reverse Transcription Kit (Applied Biosystems, USA) in accordance with the manufacturer's protocol. Each reaction employed 10 μL of equalized RNA as the template. The RT-PCR cycling conditions consisted of an initial denaturation step at 25°C for 10 min, followed by a reverse transcription step at 37°C for 120 min, and a final hold at 4°C for 5 min. The resulting cDNA was analyzed using a NanoDrop instrument and adjusted to a concentration of 10 ng/ μL in RNase-free water. The samples were stored at -20°C .

To perform real-time PCR, the reaction mixture was prepared using the PowerUp SYBR Green Master Mix kit (Applied Biosystem, USA). For one reaction, 50 ng of cDNA template, SYBR Green and 500 nM forward and reverse primers (Genomed, Poland) were composed in 15 μL . Primer sequences are given in Table 1. The reaction mixture was applied to MicroAmp™ Fast Optical 48-Well Reaction Plate (Applied Biosystems, USA) in four repetitions. The reaction was carried out on the StepOne-Plus™ Real-Time PCR System using the following thermal cycling protocol: an initial denaturation at 95°C for 10 min, followed by 40 cycles of alternating denaturation at 95°C for 15 s and annealing at 60°C for 60 s. The endogenous control used was *glyceraldehyde-3-phosphate dehydrogenase (GADPH)*, with results normalized to the calibrator and

Table 1
Primer sequences for the investigated genes.

Gene	Sequence of primer 5' → 3'	Amplicon size [bp]
<i>INGα2</i>	F: GGAACGGGACTTTTCGCAT R: GGTACTTCGGCTTTCTCATCA	154
<i>INGα3</i>	F: AAGGGACCTTCAGGTGCA R: TGTAGCCGGTGATTTACCAT	129
<i>INGα4</i>	F: GCTTCTCAGATCTGCTCGTG R: GTCACTTCCAACGAGGTTTG	131
<i>INGα5</i>	F: GCCGATTCACATCGCTCTCAAC R: GTCCTTCCACAGTCCAGCAAG	139
<i>INGα6</i>	F: TTGAATATACTGTAACCCCG R: TCGAACTGAACTCTTGAGGATAG	113
<i>INGβ1</i>	F: GGATTCTCCAGAAGGTGGTTTCG R: TGCCACCAAGTTCCCATCTCC	143
<i>E-cadherin</i>	F: ACAACGCCCCATACCAGA R: CACTCGCCCGTGTGTAGT	138
<i>B-catenin</i>	F: CCTATGCAGGGGTGTCAAC R: CGACCTGAAAACGCCATCA	95
<i>FAK</i>	F: CCCACAGAGGAGTATGTCC R: CCCAGGTCAGAGTTCAATAG	150
<i>GADPH</i>	F: GAGAAGGCTGGGGCTCATTTG R: CATGGTTCACACCATG	97

ING – integrin; *FAK* – focal adhesion kinase; *GADPH* – glyceraldehyde-3-phosphate dehydrogenase.

calculated using the 2^{-ΔΔCT} method.

2.7. Secretory profile of growth factors

To investigate the impact of cell scaffolds on the profile of growth factors, an antibody array analysis was performed at the protein level. Cell samples were prepared by seeding cells on six separate materials as described in section 2.6.2. After 24h of cultivation, the cell culture medium from each group was collected, the cells were detached, centrifuged and washed twice with PBS^{-/-}. The resulting cell pellets were resuspended in ice-cold radioimmunoprecipitation assay buffer (RIPA; Sigma-Aldrich) with Halt Protease & Phosphatase Inhibitor Cocktail and 5 mM EDTA (Thermo Fisher Scientific) and homogenized using a Cell™ Ultrasonic Liquid Processor on ice for 1 min with 5-second intervals. The samples were then left on ice for 30 min, vortexing every 15 min, followed by centrifugation at 12 000 × g and 4°C for an additional 30 min. The resulting supernatants were transferred to fresh tubes, and the protein concentration was determined using the Bicinchoninic Acid Kit (BCA; Merck Millipore, USA).

A human growth factor antibody array (ab134002, Abcam, UK) was employed for the analysis of lysates containing 250 μg of total protein in 1 mL of 1X Blocking Buffer. The procedure was carried out in accordance with the manufacturer's protocol with overnight incubations. Raw images were captured using a ChemiDoc Imaging System (Bio-Rad, USA) and subsequently analyzed using ImageJ software. Protein array images were analyzed using 'Protein Array Analyzer' plugin for ImageJ. Images were adjusted by background subtraction with rolling ball radius of 25. Results were normalized and presented as fold change relative to control.

The proteins analyzed were: amphiregulin (AREG), basic fibroblast growth factor (bFGF), epidermal growth factor (EGF), epidermal growth factor receptor (EGF R), fibroblast growth factor 4 (FGF-4), fibroblast growth factor 6 (FGF-6), fibroblast growth factor 7 (FGF-7), granulocyte colony-stimulating factor (G-CSF), glial-derived neurotrophic factor (GDNF), granulocyte-macrophage colony-stimulating factor (GM-CSF), heparin-binding EGF-like growth factor (HB-EGF), hepatocyte growth factor (HGF), insulin-like growth factor binding protein 1 (IGFBP-1), insulin-like growth factor binding protein 2 (IGFBP-2), insulin-like growth factor binding protein 3 (IGFBP-3), insulin-like growth factor binding protein 4 (IGFBP-4), insulin-like growth factor binding protein 6 (IGFBP-6), insulin-like growth factor I (IGF-I), insulin-like growth factor I receptor (IGF-I SR), insulin-like growth factor II (IGF-II), macrophage

colony-stimulating factor (M-CSF), macrophage colony-stimulating factor receptor (M-CSF R), beta-nerve growth factor (beta-NGF), neurotrophin-3 (NT-3), neurotrophin-4 (NT-4), platelet-derived growth factor receptor alpha (PDGF Ra), platelet-derived growth factor receptor beta (PDGF Rβ), platelet-derived growth factor AA (PDGF-AA), platelet-derived growth factor AB (PDGF-AB), platelet-derived growth factor BB (PDGF-BB), placental growth factor (PLGF), stem cell factor (SCF), stem cell factor receptor (SCF R), transforming growth factor alpha (TGF-α), transforming growth factor beta (TGF-β), transforming growth factor beta 2 (TGF-β2), transforming growth factor beta 3 (TGF-β3), vascular endothelial growth factor A (VEGF-A), vascular endothelial growth factor receptor 2 (VEGF R2), vascular endothelial growth factor receptor 3 (VEGF R3), vascular endothelial growth factor D (VEGF-D).

2.8. Statistical analysis

The significance of differences between groups was evaluated using one-way ANOVA, followed by Tukey's post-hoc test, with statistical analysis performed using GraphPad Prism 9.1.2 (GraphPad Software, USA). Statistically significant differences were detected at a p-value of < 0.05.

3. Results

3.1. Characterization of PLLA+GO-Au scaffold

In the present study, a PLLA+GO-Au scaffold was fabricated as presented in Fig. 1a and comprehensively characterized. FE-SEM visualization (Fig. 1b, Fig.S 1) revealed cylindrical, uniform fibers with random orientation for both PLLA and PLLA+GO-Au, without artifacts or irregular bead-like structures. The degree of homogeneity in the PLLA fiber diameter was higher compared to PLLA+GO-Au. The average diameter was 973 ± 183 nm for PLLA and 1577 ± 232 nm for PLLA+GO-Au. The surface of the PLLA fibers was smooth, while numerous nanopores, ranging from round to ellipsoidal, were visible on the PLLA+GO-Au fibers. Moreover, the results of the contact angle measurements (Fig.S 2) indicate that the contact angle for PLLA is 122 ± 2.1°, suggesting a high hydrophobicity of this material. In contrast, the addition of GO-Au to PLLA reduces the contact angle to 110 ± 2.5°.

The elemental composition of PLLA and PLLA+GO-Au was investigated using X-ray photoelectron spectroscopy (XPS), thereby enabling the evaluation of the presence of incorporated GO-Au nanocomposite into the molecular structure of PLLA fibers. The survey XPS spectrum of PLLA and PLLA+GO-Au composites displayed dominant C1s and O1s peaks (Fig. 2a). The PLLA+GO-Au additionally exhibits traces of Au4f, indicative of Au presence. The carbon content was determined to be 65.30% for PLLA and 65.39% for PLLA+GO-Au, while the oxygen content was found to be 34.70% and 34.56%, respectively. Furthermore, a notable peak was observed at the binding energy corresponding to the presence of Au in the PLLA+GO-Au composite sample, with an Au content of approximately 0.05%. This finding provides compelling evidence for the effective incorporation of GO-Au into polymer fibers.

The high-resolution XPS C1s spectra of PLLA and PLLA+GO-Au composites are shown in Fig. 2b and Fig. 2e, respectively. The C1s spectrum of both materials revealed three distinct types of carbon bonds: C-C, C-O, and O-C=O, characterized by binding energies of approximately 285 eV, 287 eV, and 289 eV, respectively. After deconvolution, the spectra showed that the percentage of C-C bonds increases from 24.15% to 24.84% for PLLA+GO-Au compared to PLLA. Concurrently, a decrease in the abundance of C-O chemical bonds (20.26% for PLLA and 20.16% for PLLA+GO-Au) and O-C=O species (20.89% for PLLA and 20.39% for PLLA+GO-Au) was observed. Furthermore, two main peaks were observed in the O1s spectrum (Fig. 2c and Fig. 2f): C=O (17.81% for PLLA and 17.86% for PLLA+GO-Au) and C-O (16.89% for PLLA and 16.70% for PLLA+GO-Au), corresponding to energies of approximately 532.5 eV and 544 eV, respectively. The XPS spectrum for Au 4f in the

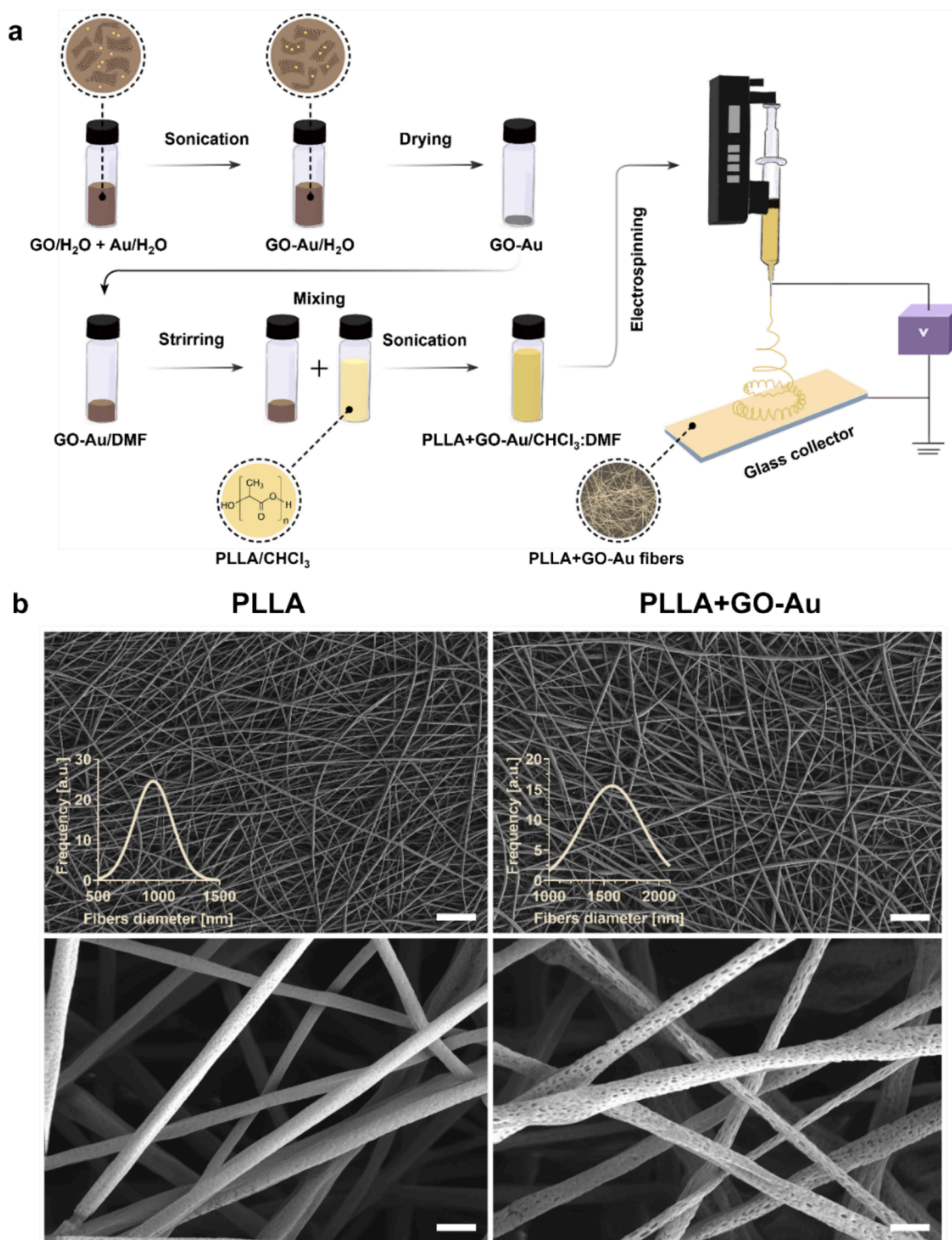


Fig. 1. (a) Schematic presentation of cell scaffolds fabrication. (b) Morphological visualization of PLLA and PLLA + GO-Au fibers using a FE-SEM along with the fiber size distribution. Scale: 20 μm and 1 μm (close ups).

case of the PLLA+GO-Au sample (Fig. 2d) can be deconvoluted into two distinct peaks. The first peak, centered at a binding energy of 85.8 eV, is attributed to neutral Au atoms associated with the presence of Au NPs, while the second peak, centered at a binding energy of 89.8 eV, corresponds to Au ions or oxides.

In order to identify structural variations and chemical bonds, Fourier Transform Infrared (FT-IR) spectroscopy was employed (Fig. 2g). Following the enrichment of PLLA with GO-Au, no discernible

differences were observed in the obtained spectra compared to the pristine polymer. The characteristic peaks of PLLA were detected, including the C=O ester carbonyl stretch at 1754 cm^{-1} , the C-O-C stretch at 1185 cm^{-1} , and the C-O stretch at 1087 cm^{-1} . Additional, less prominent peaks corresponding to PLLA were also discernible. In the region between $3000\text{--}2900\text{ cm}^{-1}$, two peaks were assigned to asymmetric and symmetric C-H stretching vibrations. In the range of $1500\text{--}1300\text{ cm}^{-1}$, peaks were detected at 1450 cm^{-1} , 1380 cm^{-1} , and

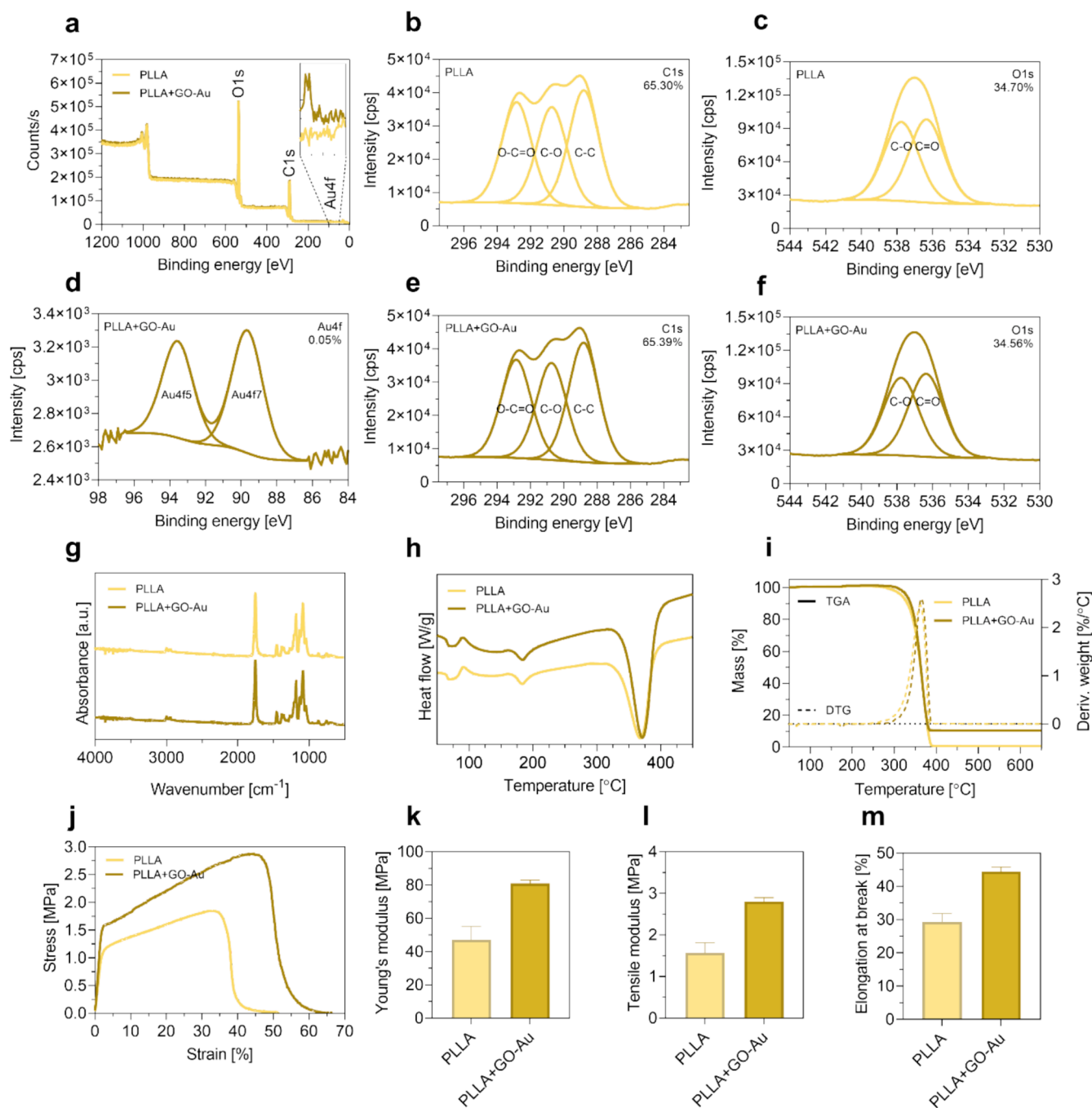


Fig. 2. Physical-chemical analysis of PLLA and PLLA + GO-Au. Elemental composition: (a) full survey XPS spectrum, XPS high-resolution spectrum of (b) C1s and (c) O1s for PLLA and (d) Au4f, (e) C1s and (f) O1s for PLLA + GO-Au. (g) FT-IR spectra. Thermal properties: (h) DSC heating and (i) DSC/TGA thermograms. Mechanical properties: (j) stress–strain curve, (k) Young's modulus, (l) tensile strength, (m) elongation at break.

1362 cm^{-1} , corresponding to C-H deformation modes (asymmetric bend, symmetric bend, and bend, respectively). Furthermore, three additional peaks were identified as C-O stretching vibrations at 1267 cm^{-1} , 1129 cm^{-1} , and 1044 cm^{-1} . Additionally, peaks associated with C-C stretching at 868 cm^{-1} and C-H rocking vibration at 755 cm^{-1} were also observed.

Structural changes in the chemical and physical properties presented as a function of temperature were investigated to elucidate the impact of GO-Au on the thermal properties of PLLA by employing differential scanning calorimetry (DSC) analysis (Fig. 2h). The DSC heating thermograms of PLLA and PLLA+GO-Au nanocomposites exhibited two endothermic peaks, corresponding to the glass transition temperature

(T_g) and melting temperature (T_m), as well as an exothermic peak of cold crystallization temperature (T_c). The T_g value for PLLA+GO-Au was found to be 72.48°C , indicating a 1.45°C increase compared to that of pure PLLA. Conversely, a discrete decrease in T_c was detected for PLLA+GO-Au, which was 90.61°C , representing a 0.1°C reduction compared to the PLLA sample. A slight increase in T_m was observed for PLLA+GO-Au, recorded at 184.19°C , which is 0.17°C higher than that of PLLA, with a T_m of 184.02°C .

Concurrent thermal degradation behavior was observed for PLLA and PLLA+GO-Au composite samples upon heating, as revealed by thermogravimetric analysis (TGA) and derivative thermogravimetric analysis (DTG) curves (Fig. 2i). No significant changes in the sample's

composition or structure were observed up to 280°C, indicating its thermal stability up to this temperature. The primary mass loss occurred within the temperature range of 300–400°C. The thermal stability of the materials is reflected in their respective peak decomposition temperatures, at 362.38°C for PLLA and 365.54°C for PLLA+GO-Au. Notably, the PLLA sample exhibited near-complete decomposition, with only 0.47% of the initial mass remaining above 600°C. In contrast, the PLLA+GO-Au composite retained 10.37% of its initial mass at elevated temperatures.

The mechanical properties of PLLA and PLLA+GO-Au composites were investigated, and the results are presented in Fig. 2j–m. Young's modulus, a measure of the material's stiffness, was found to be 47 ± 8 MPa for PLLA and 81 ± 2 MPa for PLLA+GO-Au, indicating a significant improvement in mechanical properties. The tensile strength, which is a maximum stress that material can withstand while being stretched, was found to be 1.6 ± 0.3 MPa for PLLA and 2.7 ± 0.1 MPa for PLLA+GO-Au. Furthermore, the elongation at break, which is a measure of a material's ductility, was found to be 29% for PLLA and 44% for PLLA+GO-Au.

3.2. Biocompatibility of PLLA+GO-Au scaffolds *in vitro*

Mitochondrial activity and cellular viability were evaluated in cells cultured on cell scaffolds using the XTT assay. The results indicated that HEKa cells (Fig. 3b) grown on PLLA substrates exhibited significant impairment in metabolic activity at both 24 h (82%) and 72 h (85%). HEKa cells seeded on PLLA+GO-Au demonstrated a transient decline in viability at 24 h, followed by recovery to 104% of control levels at 72 h. Notably, HFFF2 cells (Fig. 3c) cultured on PLLA displayed initial viability equivalent to controls (95%) at 24 h, only to decline significantly to 58% after 72 h. Conversely, HFFF2 cells maintained on PLLA+GO-Au surfaces exhibited enhanced mitochondrial activity at both 24 h (120%) and 72 h (149%).

The biocompatibility assessment of cell scaffolds was further substantiated by the evaluation of lactate dehydrogenase (LDH) release. Statistical analysis revealed no significant increase in LDH release for HEKa cells, except for those cultured on PLLA scaffolds for 24 h (Fig. 3d). Similarly, HFFF2 cells exhibited elevated LDH release after 72 h of cultivation on PLLA+GO-Au scaffolds (Fig. 3e). This phenomenon may be attributed to an increase in cellular density on the material, which is consistent with enhanced mitochondrial activity inferred by XTT test results. In both instances, the LDH release was slightly overestimated, with values exceeding 7% and 8% cytotoxicity for the HEKa and HFFF2 cells, respectively.

In order to complete the biocompatibility panel at the cellular level, a preliminary visualization of cell colonization of the biomaterial was made (Fig. 3f). The visualization of cell settlement after 24 h revealed a significantly lower number of HEKa cells on the PLLA surface, with the majority exhibiting rounded morphology, compared to the PLLA+GO-Au surface, which showed a higher number of cells displaying a more flattened morphology. Following 72 h, the PLLA surface demonstrated an increase in HEKa cell density, with cells exhibiting a more pronounced flattening. In contrast, the PLLA+GO-Au surface displayed a substantially higher HEKa cell density, with cells covering nearly the entire surface and forming a compact layer. Furthermore, the cell growth exhibited three-dimensional characteristics reminiscent of epidermal growth, characterized by upward proliferation and cell–cell interactions, which are hallmarks of this specific type of growth pattern. The morphological analysis of HFFF2 cells cultured on PLLA and PLLA+GO-Au surfaces revealed distinct differences between the two scaffolds. After 24 h, cells with normal morphology were observed on both surfaces, with a slightly higher density on PLLA+GO-Au compared to neat PLLA. In contrast, after 72 h, a significant reduction in cell number was observed on PLLA compared to the 24-hour time point, accompanied by the formation of clusters and rounded cells, which is not typical of this cell line. Conversely, HFFF2 cells on PLLA+GO-Au

exhibited normal growth and proliferation, with a higher cell density compared to the same material after 24 h.

To complement the biocompatibility panel with a tissue model, the EpiDerm™ model was used (Fig. 4), which architecturally reproduces the epidermis *in vivo*. The model is composed of basal, spinous, granular, and stratum corneum layers (Fig. 4a) derived from human keratinocytes. It fits perfectly into the implementation of the 3R principle (replacement, reduction, refinement), enabling research without the use of an animal model and, at the same time, ensuring greater complexity of interactions between cells in spatial tissue compared to cell models.

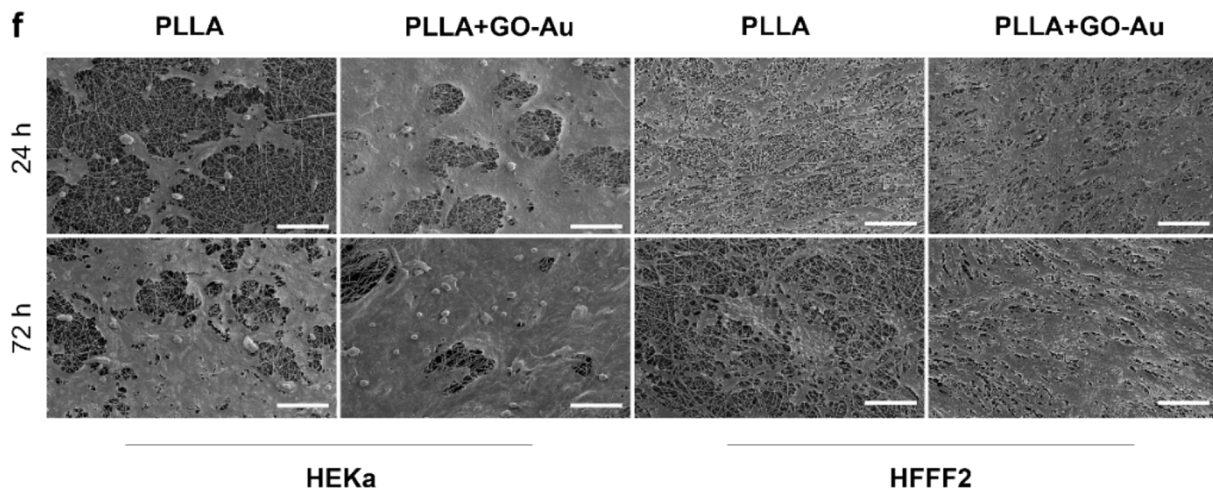
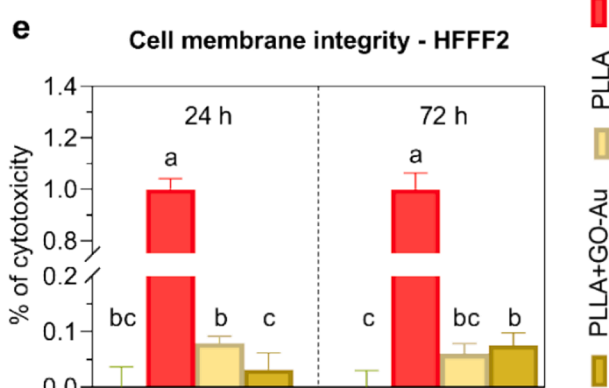
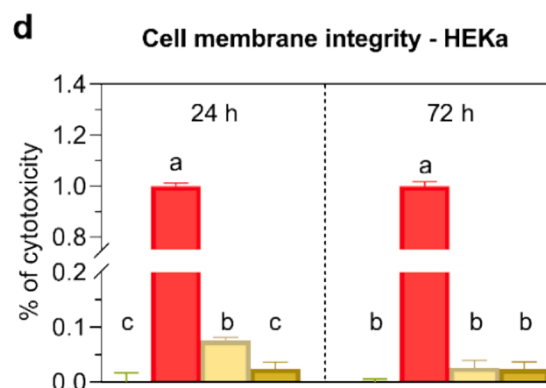
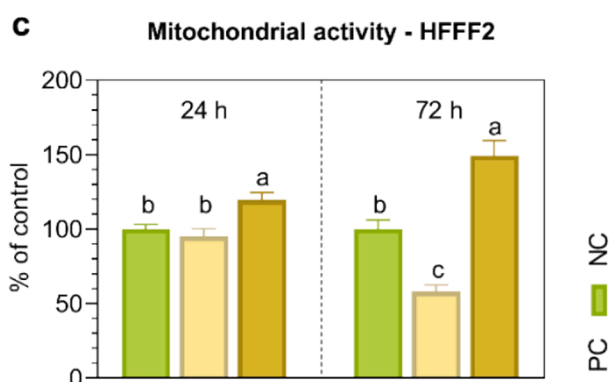
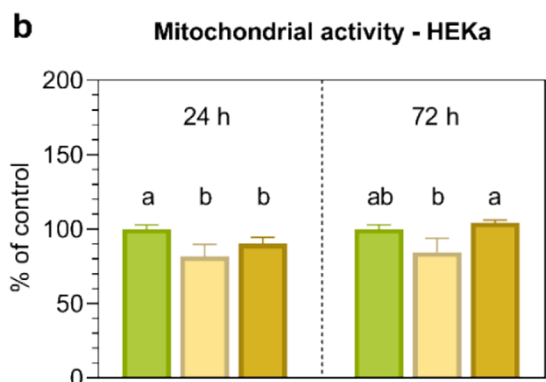
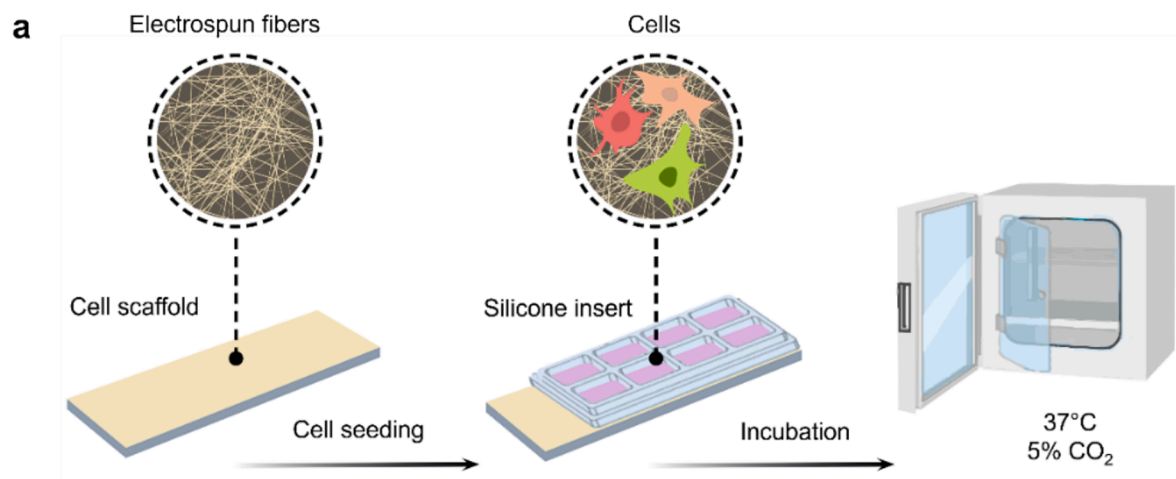
The cytotoxicity assessment (Fig. 4b) revealed a significant increase in LDH release in the tissue treated with neat PLLA, indicating cell membrane perforation, with levels increasing to 148%, 133%, and 197% compared to NC (100%) after 24h, 48h, and 72h, respectively. Conversely, the tissue in direct contact with PLLA+GO-Au at each time point demonstrated reduced LDH release to 86%, 74%, and 70% compared to NC for 24h, 48h, and 72h, respectively. These findings suggest that the combination of PLLA and GO-Au may exhibit improved biocompatibility compared to neat PLLA.

Histological analysis revealed that the cell scaffolds, comprising both PLLA and PLLA+GO-Au, did not exert a detrimental impact on tissue architecture (Fig. 4c). No disruptions to tissue continuity, necrotic processes, or increases in tissue porosity were observed, in contrast to the PC control group. Following 72 h of exposure to the biomaterials, four distinct layers characteristic of the epidermis remained intact. The stratum corneum was composed of flat, large anucleated cells. The granular layer exhibited spindle-shaped cells with their long axis oriented parallel to the epidermal surface, featuring granules comprising keratohyalin and keratinosomes. The spinous and basal layers were characterized by flattened or cuboidal cellular morphology. Morphometric analyses revealed changes in layer thickness and tissue porosity after 72 h of contact with the scaffolds (Fig. 4d–f). The tissue exposed to PLLA demonstrated an increase in stratum corneum thickness. In contrast, the tissue treated with PLLA+GO-Au exhibited thicker layers of stratum corneum and stratum germinativum, accompanied by a decrease in stratum corneum porosity. Furthermore, the hemolysis analysis demonstrated the hemocompatibility of the scaffolds, both PLLA and PLLA+GO-Au, where the percentage of hemolysis was comparable to that of the negative control, remaining below 1% (Fig.S 3).

3.3. The influence of PLLA+GO-Au scaffold on cell morphology

Visualization of the actin cytoskeleton, nuclear morphology, and cellular morphology was achieved through the utilization of confocal microscopy and scanning electron microscopy (Fig. 5).

The morphological analysis of HEKa cells grown on PLLA substrates revealed a significant diminution of actin filament length, accompanied by a corresponding decrease in the spatial extent of the actin cytoskeleton, suggesting the occurrence of cellular shrinkage and reorganization. The three-dimensional reconstructed image provided an orthogonal view, which revealed that HEKa cells on PLLA formed an irregular cytoskeletal layer with a thickness comparable to that of control cells, indicating a similar structural organization. However, the thinning of the nuclear layer may suggest impaired colonization of the PLLA scaffold by keratinocytes. In contrast, cells cultured on PLLA+GO-Au exhibited elongated protrusions composed of densely packed actin filaments, anchoring them to the scaffold pores. The HEKa cell cytoskeleton displayed mild cytoskeletal stresses in response to the three-dimensional environment. HEKa cells inhabited the PLLA+GO-Au scaffold at multiple levels, as evidenced by a significantly thicker actin layer compared to control and PLLA-treated cells. On both the PLLA and PLLA+GO-Au scaffolds, cell nuclei with typical morphology from round to ellipsoidal, similar to control cells, were observed without the sign of the apoptotic bodies. SEM visualization revealed the presence of HEKa cells both on the surface of fibers and under individual fibers indicating effective cellular integration with the scaffolds. Cells formed filopodia



(caption on next page)

Fig. 3. Biocompatibility assessment of PLLA and PLLA + GO-Au cell scaffolds at the cellular level. (a) Schematic representation of a methodology for the direct evaluation of the biocompatibility of cellular scaffolds after 24 h and 72 h incubation. (b, c) Cell viability analysis by assessing mitochondrial enzyme activity using the XTT assay. (d, e) Evaluation of scaffold cytotoxicity by assessing LDH release. The results are expressed as a percentage of the negative control (NC) for XTT or a percentage of cytotoxicity for LDH in comparison to PC (positive control) and NC (mean with standard deviation; $n = 5$). Different letters above the bars indicate statistically significant differences among the groups ($p \leq 0.05$). (f) Scanning electron microscopy visualization of PLLA and PLLA + GO-Au colonization by HEKa and HFFF2 cells; scale: 100 μm .

not only relative to the scaffold but also to each other, leading to the formation of compact cellular structures characteristic of epidermal tissues.

In the case of HFFF2 cultured on biomaterials, cell growth was found to be influenced by the geometry and organization of the fibers within the material. The actin cytoskeleton in scaffolds-treated cells exhibited a more compact structure than control cells, with cells adhering directly to the polymer fibers. Cytoskeletal and nuclear layers of cells cultured on PLLA exhibited thicknesses comparable to those of control cells. Moreover, cells cultured on PLLA scaffold exhibited elongated nuclei and a limited number of apoptotic bodies, indicating a cytotoxic effect of PLLA. This observation is consistent with the results of cytotoxicity tests (Fig. 3). In contrast, an increase in both nuclear and cytoskeletal layer thickness was observed in cells cultivated on PLLA+GO-Au. Consistent with the observations in cells treated with PLLA, elongated nuclei were identified in cells subjected to PLLA+GO-Au treatment; notably, this observation occurred in the absence of apoptotic bodies.

3.4. Proadhesive properties of PLLA+GO-Au scaffold evaluation

The kinetics of cell adhesion to cell scaffold surfaces were investigated by seeding cells onto control and biomaterial surfaces. Non-adherent cells were removed at specific time points, allowing for the quantification of cell nuclei per square millimeter and subsequent determination of adherent cells (Fig. 6a). For HEKa cells, no significant differences in adhesion were observed between the pure PLLA surface and the control surface at 60 min and 480 min. However, at 120 min and 240 min, more cells were observed on the PLLA surface than the control surface. In contrast, the PLLA+GO-Au scaffold exhibited stable cell adhesion, as evidenced by the significantly increased number of adherent cells compared to both control and PLLA surfaces. For HFFF2 cells, the data indicate that after 60 min and 480 min, the scaffolds demonstrated proadhesive properties, with a higher number of cells observed on these surfaces compared to the control surface. Moreover, a more significant number of cells was seen on the PLLA+GO-Au scaffold at 120 min and 240 min compared to both control and neat PLLA.

To elucidate the molecular mechanisms underlying the kinetic curves and proadhesive properties of cell scaffolds enriched with GO-Au, real-time PCR analysis was conducted to investigate the expression of selected cell adhesion molecules (CAMs). The HEKa cell line (Fig. 6b) displayed a significant upregulation of *INGa3*, *INGa6*, *INGb1*, and *E-cadherin* when cultured on PLLA and PLLA+GO-Au substrates. Moreover, *FAK* expression was found to be upregulated in HEKa cells on PLLA, while *INGa4* expression was specifically upregulated in cells on PLLA+GO-Au. In contrast, *INGa5* was downregulated only in HEKa cells cultured on PLLA. HFFF2 cells (Fig. 6c) cultivated on both PLLA and PLLA+GO-Au scaffolds exhibited upregulation of *INGa3*, *INGa4*, *INGb1*, *E-cadherin*, and β -*catenin*. Notably, PLLA+GO-Au substrates also led to the upregulation of *INGa5* and *FAK*, as well as the downregulation of *INGa2*.

3.5. The influence of the PLLA+GO-Au scaffold on the secretion profile of growth factors

To evaluate the proregenerative properties of cell scaffolds, the secretion of GFs was analyzed (Fig. 7). The most substantial increases in secretion by HEKa cells, especially in the context of skin regeneration, were detected for amphiregulin (AREG), basic fibroblast growth factor

(bFGF), epidermal growth factor (EGF), and epidermal growth factor receptor (EGF R) (Fig. 7b). In HEKa cells cultured on neat PLLA (Fig. 7b), the secretion levels of AREG, bFGF, EGF and EGF R were observed to increase by factors of 3.9, 2.7, 1.2, and 2.8, respectively, in comparison to the control. Remarkably, cells cultivated on PLLA+GO-Au exhibited significantly greater increases in the secretion levels of AREG, bFGF, EGF and EGF R by factors of 6.3, 7.3, 3.1, and 6.1, respectively, compared to the control cells. The analysis indicated that the HFFF2 cells exhibited smaller variations in the secretory profile when compared to the HEKa cells (Fig. 7a). The most significant enhancement in the synthesis of HFFF2 by the cells, in comparison to the control, was observed for bFGF and EGF R (Fig. 7c). Nevertheless, the level of secretion was reported to be 1.4 to 1.6 times higher, indicating a relatively modest change.

4. Discussion

The development of electrospun scaffolds integrated directly with cells, alongside the modulation of targeted cellular responses to promote skin regeneration, represents a promising therapeutic approach in the field of cell therapy. A significant challenge in the design of cell-enriched scaffolds lies in achieving precise coordination and effective communication between the scaffold and the cells, as this interaction is fundamental to establishing a successful biointerface.

Numerous substances such as hyaluronic acid and collagen have demonstrated positive effects on cell adhesion and proliferation, but their animal-derived origins introduce risks, including immunological reactions and ethical concerns. PLLA embedded with GO-Au, providing a synthetic alternative that eliminates these risks and enhances biocompatibility. Significantly, our biomaterial selectively stimulates keratinocytes to secrete growth factors, while fibroblasts remain unresponsive. This selective interaction supports tissue regeneration and minimizes scar formation by promoting a more organized healing process. By controlling the activation of specific cell types, our approach presents distinct advantages in tissue engineering and regenerative medicine. In summary, our work highlights the potential of PLLA and GO-Au to improve cell adhesion and functionality in regenerative applications without the complications associated with biological materials.

Our findings elucidate the impact of incorporating the GO-Au on the modification of the nanostructure of PLLA fibers (Fig. 1b). Nanopores on the surface of fibers can be generated through the application of a highly volatile solvent in conjunction with elevated humidity levels [36], or by employing a binary solvent system consisting of a good solvent and a non-solvent with higher boiling point [37]. This phenomenon may also be attributed to differences in the evaporation rates of the solvents involved. It is well established that DMF exhibits a lower evaporation rate compared to CHCl_3 . Furthermore, GO can engage in interactions with DMF [38], which may inhibit the mobility of DMF molecules and consequently decelerate the evaporation of the solvent. Manipulation of the nanotopography has the potential to influence various properties of the cellular scaffold, thus exerting significant effects on its biological performance.

The incorporation of the GO-Au nanocomposite into the PLLA matrix did not induce any alterations in the chemical structure (Fig. 2g); however, it resulted in subtle enhancements in the thermal properties (Fig. 2h,i) and significantly improved the mechanical properties (Fig. 2j-m) of the material. The increased T_g and T_m of PLLA+GO-Au (Fig. 2h)

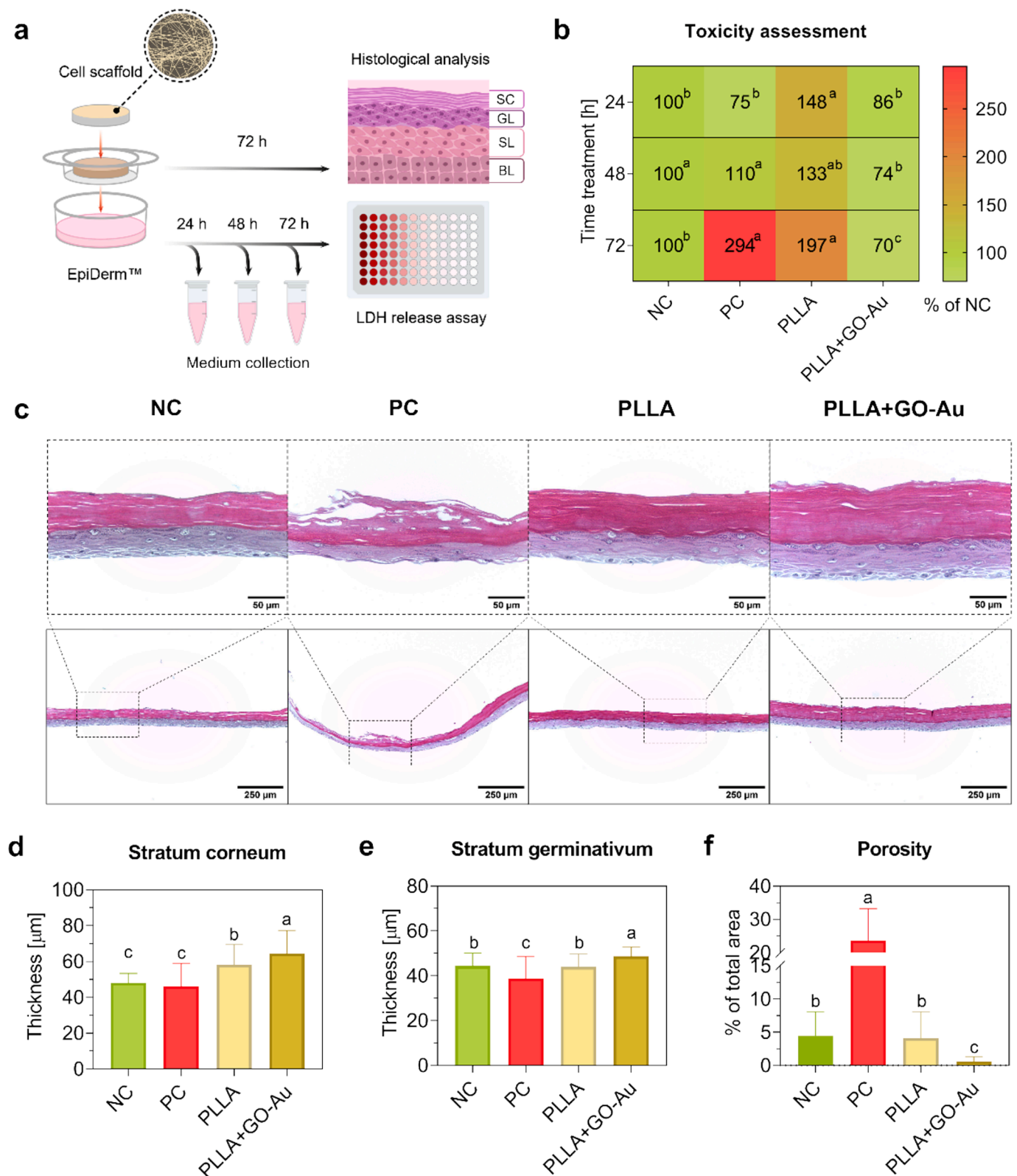


Fig. 4. Evaluation of the biocompatibility of PLLA and PLLA + GO-Au scaffolds utilizing the EpiDerm™ model. (a) A schematic representation demonstrating the evaluation of biocompatibility of scaffolds, complemented by an illustration of the histological architecture of the tissue model: stratum corneum (SC), granular layer (GL), spinosum layer (SL), and basal layer (BL). (b) Toxicity assessment of biomaterials determined by lactate dehydrogenase (LDH) release test after 24, 48 and 72 h of incubation. Results are reported as a percentage of the negative control (NC), with data expressed as mean ± standard deviation (n = 5). (c) Histological evaluation post-72-hour incubation with scaffolds performed using hematoxylin-eosin staining (scales: 50 μm (zoom), 250 μm); morphometric assessment of (d) stratum corneum thickness, (e) stratum germinativum thickness and (f) porosity. Results are presented as mean ± standard deviation (n = 80). Different letters above the bars indicate statistically significant differences among groups (p ≤ 0.05).

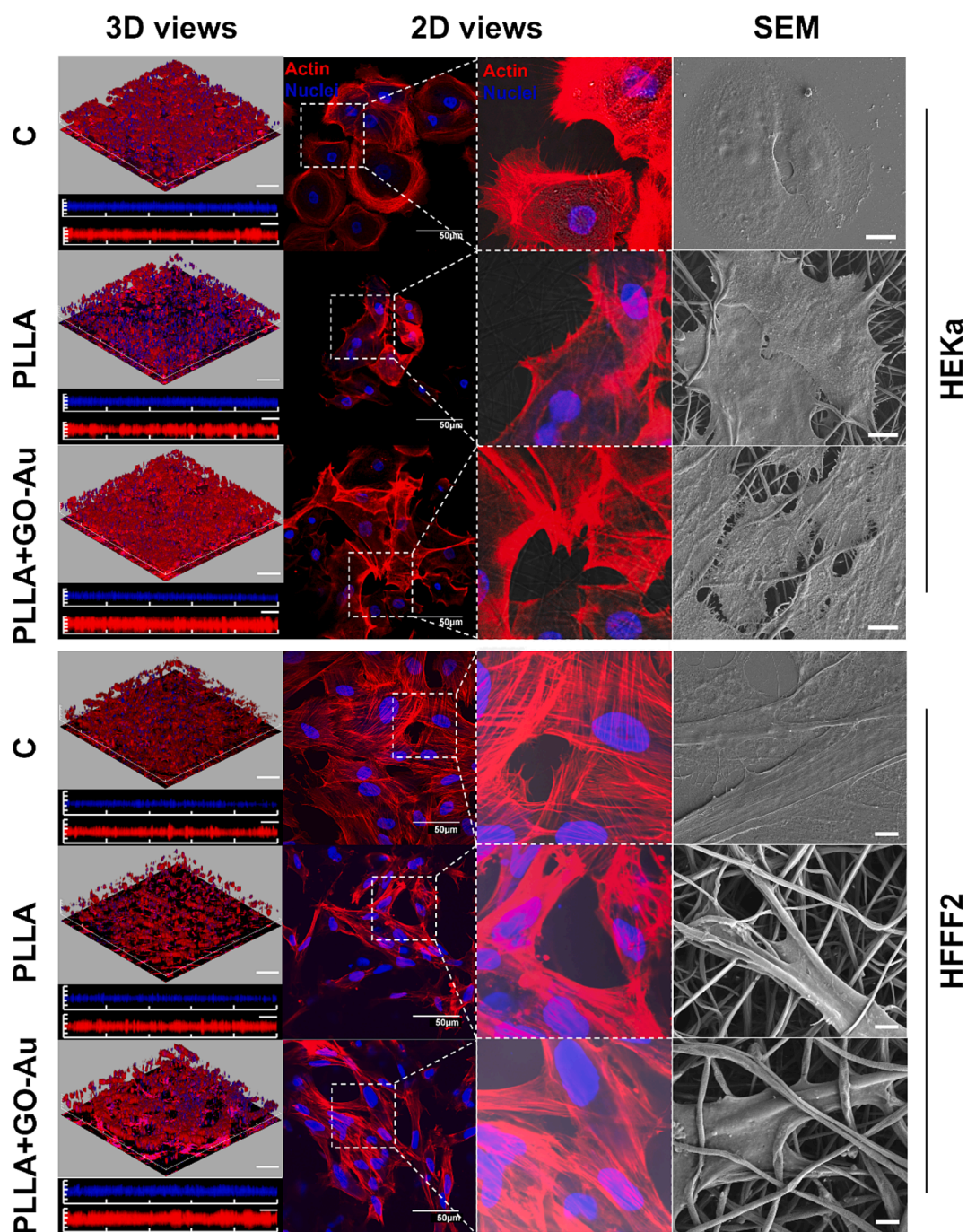


Fig. 5. Detailed visualization of the morphology of HEKa and HFFF2 cells after 24 h of cultivation on PLLA and PLLA + GO-Au scaffolds). Imaging with confocal microscopy and FE-SEM. Three-dimensional analysis of scaffold colonization by cells with an orthogonal projection on cell nuclei (blue layer) and actin cytoskeleton (red layer); scales: 220 μm (3D view), 110 μm (orthogonal view). Two-dimensional visualization of the architecture of the cell nucleus and the actin cytoskeleton (scale: 50 μm) and direct analysis of cell-fiber interactions (scale: 10 μm (HEKa), 3 μm (HFFF2)).

can be attributed to the restriction of segmental chain mobility caused by the incorporation of GO-Au [39], which exhibits electrostatic interactions, and undergoes mechanical hindrance [40]. Interactions between GO-Au nanocomposite and the PLLA matrix likely restrict the free rotation and translation of polymer chains, resulting in a slight stiffening of the polymer matrix and hindering polymer chain mobility and relaxation. The observed enhancement in thermal stability of nanostructured scaffold (Fig. 2i) can be attributed to the GO nanoflakes, which act as a barrier, hindering the release of degradation products and reducing heat transfer [41]. GO's thermal conductivity allows it to efficiently dissipate heat from the polymer surface, reducing the

likelihood of melting by transferring heat away from the polymer chain motions [42]. The incorporation of GO into polymer matrices results in a substantial enhancement of the mechanical properties of biomaterials, attributed to the complex structural and chemical interactions facilitated by GO. The exceptional stiffness and strength of GO serve to reinforce the composite material, while its high surface area enhances contact with the polymer matrix, thus improving load transfer efficiency [43]. Furthermore, GO facilitates the filling of defects within the polymer, thereby reducing local stress concentrations and augmenting durability [44]. It also promotes organized crystallization within the polymer, leading to improved molecular alignment [45]. A critical

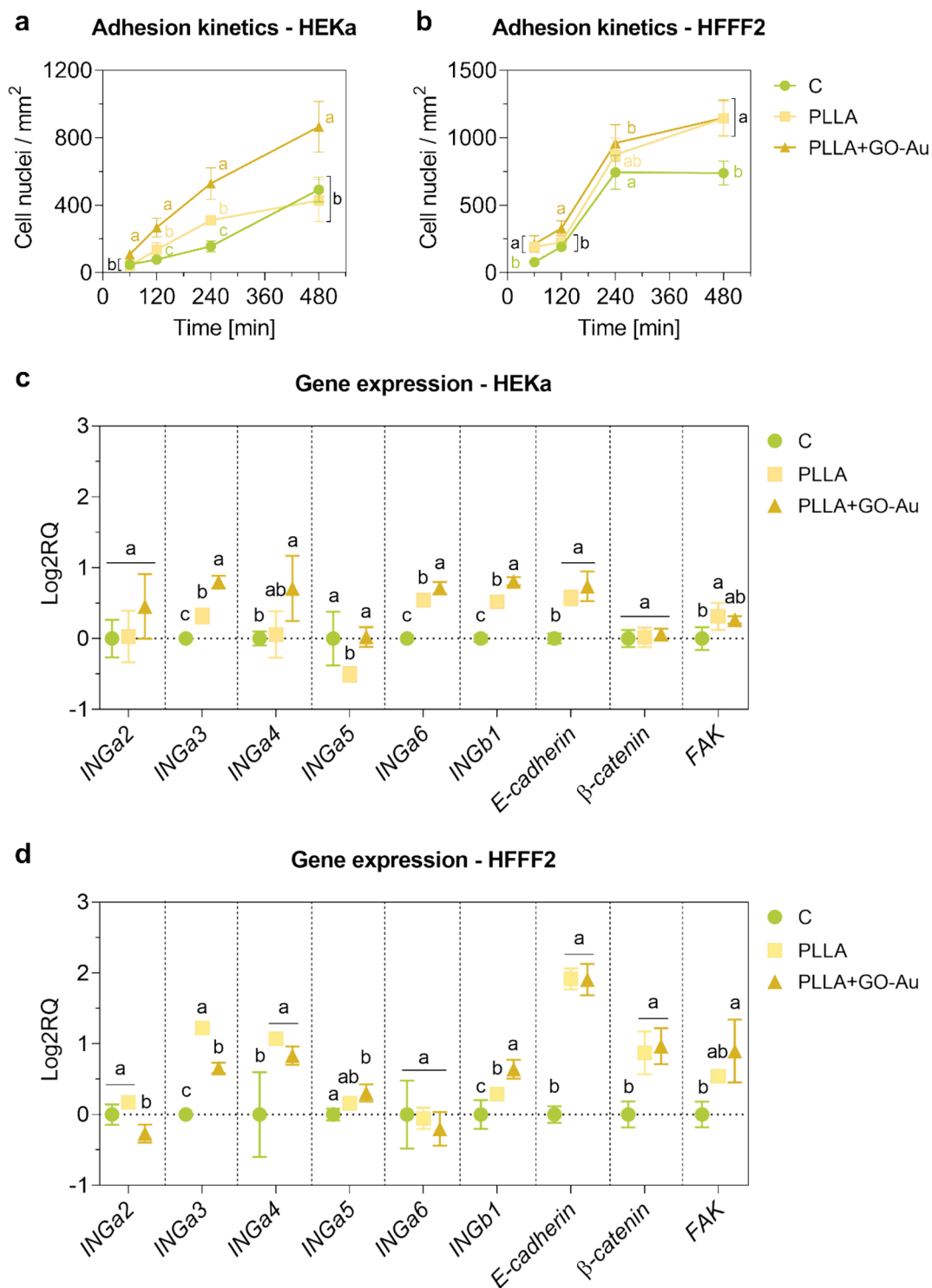


Fig. 6. Analysis of the adhesive properties of PLLA and PLLA + GO-Au scaffolds. Adhesion kinetics curves of (a) HEKA and (b) HFFF2 cells after 60 min, 120 min, 240 min, and 480 min after seeding on biomaterials assessed by visualization and counting of cell nuclei using a confocal microscope. The results are expressed as cell nuclei/mm² (mean with standard deviation; n = 8). Different letters above the bars indicate statistically significant differences among the groups ($p \leq 0.05$). Analysis of the expression of selected integrins (*ING*), *E-cadherin*, β -*catenin* and *focal adhesion kinase* (*FAK*) at the mRNA level using real-time PCR for (c) HEKA and (d) HFFF2 cells after 24 h scaffold-treatment. Results are presented as log₂RQ (mean with standard deviation; n = 4). Different letters above the bars indicate statistically significant differences among the groups ($p \leq 0.05$).

mechanism underlying these enhancements is the improved inter-flake stress transfer resulting from various bonding interactions, including covalent bonds between the polymer and GO, as well as van der Waals and hydrogen bonds [46]. These interactions effectively distribute applied stress throughout the composite, contributing to increased

strength and resilience. The degree of GO aggregation within different polymer matrices significantly influences mechanical characteristics; a more uniform dispersion of GO correlates with enhanced load transfer and overall mechanical performance [47]. Moreover, the introduction of polymer chains into the interlayer spaces of GO not only stabilizes the

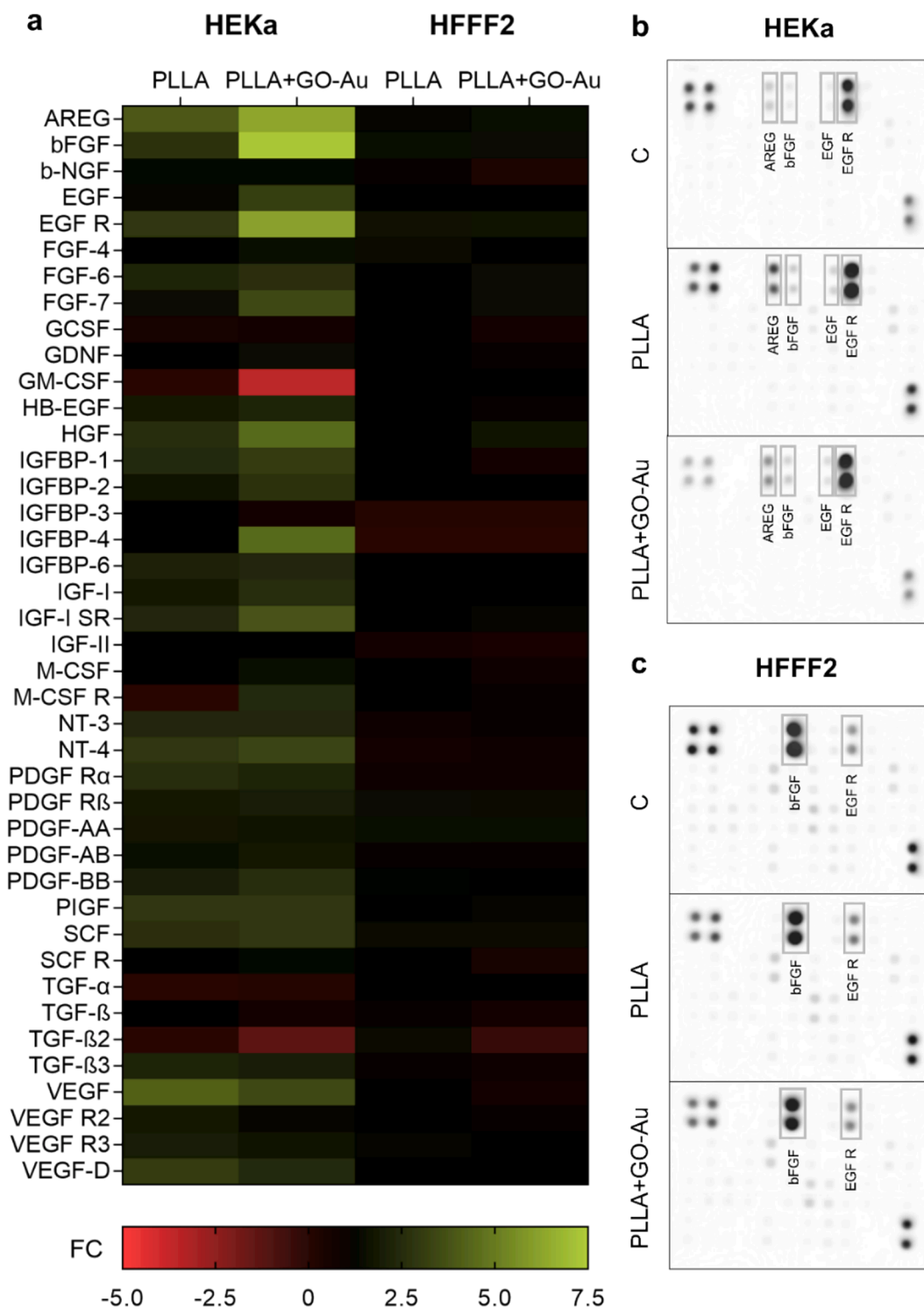


Fig. 7. Analysis of the secretion profile of cell growth factors after 24 h of direct contact with PLLA and PLLA + GO-Au. (a) Heat map expressing the relative secretion of selected growth factors based on microarray visualization of the membrane for (b) HEKa and (c) HFFF2 cells after densitometry analysis. The results are presented as fold change (FC), where the green color indicates an increase in protein secretion and red indicates a decrease in protein secretion compared to the control, designated as black (FC = 1).

dispersion but also strengthens the cooperativity of the hydrogen-bonding network [48]. The structural integrity of GO/polymer composites is crucial for their mechanical performance, as the irregular, coarse, and multi-plane fracture surfaces in GO nanocomposites indicate enhanced toughness that impedes crack propagation, with the two-dimensional nature of GO sheets effectively deflecting cracks and improving energy absorption during deformation [49].

Biocompatibility assessment of cell scaffolds is a crucial aspect of characterizing the biological properties of a biomaterial. The biocompatibility evaluation can be approached *via* two distinct methodologies: direct and indirect. The indirect method involves the preparation of an extract by incubating the biomaterial in an appropriate medium, typically a buffer or culture medium, in accordance with established ISO standards 10993-12. In contrast, the direct method entails seeding cells

onto the biomaterial, enabling a thorough evaluation of cellular behavior in direct contact with the material. This approach accounts for the surface topography and mechanical properties, closely mimicking the *in vivo* tissue conditions.

PLLA is commonly regarded as a biocompatible polymer at the cellular level, exhibiting minimal adverse effects on cell viability and function [18,50,51]. However, depending on the form and biological target, PLLA can potentially elicit cytotoxic responses, necessitating the incorporation of additives that enhance its biological behavior [52,53]. In our study, we observed a significant decrease in the mitochondrial activity of HFFF2 cells cultured in neat PLLA for 72 h (Fig. 3c). Furthermore, we have characterized the hemocompatibility of both the PLLA scaffolds and the PLLA+GO-Au composites (Fig.S 3). Our findings indicate that these materials exhibit favorable interactions with blood components, suggesting their potential suitability for applications in biomedical fields where biocompatibility with blood and surrounding tissues is essential. However, reductions in metabolic activity may have been attributed to temporary mitochondrial dysfunction caused by cellular adaptation to the new microenvironment [54]. The enhancement of the biocompatibility of PLLA by incorporating GO-Au into fibers structure, as demonstrated in our research (Fig. 3), is in line with previous findings in the literature [55–57].

The incorporation of GO-Au into the PLLA scaffold leads to enhanced biocompatibility at the tissue level, primarily attributed to the improved mechanical properties of the biomaterial, as we demonstrated in Fig. 4b. The epidermis exhibits anisotropic and viscoelastic properties, with Young's modulus varying depending on the tissue layer, as well as skin conditions [58]. The value of Young's modulus can be expected to oscillate within the range of 5–140 MPa [59]. Notably, the stratum corneum, which was in direct contact with the biomaterial in our study (Fig. 4), demonstrates the highest Young's modulus across the skin layers [60]. A mechanical mismatch can induce cellular stress, which may ultimately lead to cell death [61]. The nanotopography of PLLA+GO-Au and the numerous pores on its fiber surface may mitigate stress concentration points within the material, resulting in a more uniform distribution of stress and strain [11].

The cytoskeleton is dynamic network of proteins that provides structural support and mechanical resistance to the cell. The cytoskeletal architecture is determined primarily by the cell growth surface and exerts a direct impact on mechanosensing [62]. To ensure a precise interpretation of the visualization results, it is imperative to consider the specific conditions governing cell maintenance and their relationship to the *in vivo* tissue microenvironment. Stiffer nonwovens with larger fiber diameters induce the formation of significantly higher stress fiber density [63], which corresponds to the obtained results for HEKa cells (Fig. 5), and may indicate a structural adjustment in response to the mechanical properties of the growth niche. Keratinocytes are characterized by a remarkable stiffness, exhibiting a mechanical rigidity significantly higher than other cell types [64]. This increased stiffness is primarily attributed to the robust and deformable keratin cytoskeleton, which plays a crucial role in the skin's protective function. The geometry of electrospun nonwoven fibers influence the formation of direction-dependent actin cytoskeleton bundles in fibroblast-like cells, as demonstrated on HFFF2 cells cultivated on scaffolds (Fig. 5). This, in turn, affects the cellular response as a result of the intricate interplay between cell-matrix interactions and cytoskeletal dynamics [65]. The rearrangement of the cytoskeleton, particularly actin filaments, plays a crucial role in mediating cell shape changes and nuclear elongation, phenomena that frequently occur in cells cultured on electrospun materials with aligned fiber orientations [66].

A well-engineered cellular scaffold can regulate cell adhesion in a controlled and precisely defined manner, primarily through mechanotransduction mechanisms induced by the scaffold's mechanical properties. The establishment of an effective biointerface facilitates interactions between cell surface proteins and the biomaterial surface, resulting in the formation of stable adhesion *foci* that anchor the cells to

the scaffold. The observed enhancements in the proadhesive properties of the PLLA+GO-Au nanocomposite (Fig. 6a) underscore its potential applicability across diverse biomedical contexts. However, a comprehensive molecular elucidation of these phenomena is still required to fully understand the underlying mechanisms. Thus, we performed molecular analyses to investigate these processes and identify the key interactions and pathways involved (Fig. b,c). We demonstrated that the upregulation of integrins, as well as E-cadherin and β -catenin and FAK by the cells, unequivocally substantiates the proadhesive properties of PLLA+GO-Au (Fig. 6b,c). Integrins (INGs) are transmembrane glycoprotein receptors crucial for cell-ECM connections [67], E-cadherin and β -catenin are key molecules for cell-cell adhesion [68], while focal adhesion kinase (FAK) mediates cell adhesion *via* integrins and regulates cell flattening [69].

Extensive research has demonstrated that the incorporation of GO into the matrix of neat PLLA markedly enhances its proadhesive properties, a conclusion substantiated by studies utilizing diverse cellular models, including dental pulp stem cells [70], Schwann cells [71] and bone marrow-derived stem cells [56]. Proadhesive properties of GO can be largely ascribed to the elevated reactivity of GO, a characteristic that stems from its rich assortment of functional groups. These functional groups enhance the capacity for chemical bond formation and intermolecular interactions with the amino acids constituting proteins [72] and lipids [73] within cellular membranes. Cells can sense mechanical stimuli from the GO nanoflakes and translate them into biological responses, which may include alterations in the regulation of protein secretion profiles [74], changes in the expression levels of specific genes [75] or modifications to cytoskeletal architecture [76].

As mentioned above, the PLLA+GO-Au composite scaffold exhibits substantial proadhesive potential. It is attributed in part to the unique nanotopography of the polymer fibers (Fig. 1b), which feature a heterogeneous arrangement of nanopores conducive to protein adsorption and the formation of an organic layer. This nanotopography facilitates the development of a functional biointerface that initiates mechanotransduction events between the cells and the growth surface [77], promoting cellular integration with the growth surface. Numerous studies have established that the nanostructuring of biomaterials can significantly augment cell adhesion by upregulating ING expression [78] and FAK expression [79]. Additionally, the incorporation of secondary features such as nanopores within the fiber architecture may further influence the expression of E-cadherin [80], while facilitating the formation of multilayer cellular construct [37]. Supported cell adhesion is critically significant due to the intricate interplay between cell adhesion molecules (CAMs) and growth factors, as well as the reciprocal establishment of signaling pathways that govern protein-protein interactions, ultimately facilitating the elicitation of the desired cellular response [81].

During the process of tissue growth, a multitude of intricate biological mechanisms are engaged, including the secretion of growth factors (GFs) by cells. Ensuring the harmonization of specific protein secretion by distinct cell populations is essential to mitigate the risk of developing hypertrophic tissues, while simultaneously forming physiologically functional tissue. Our study evaluated the secretion of growth factors by cells cultured on scaffolds, with the most significant differences noted for the AREG, bFGF, EGF and EGF R (Fig. 7). AREG is particularly important in keratinocyte proliferation and T cell activation [82], bFGF stimulates fibroblast division and the formation of blood vessels [83], while EGF and its receptor EGF R coordinates cell proliferation and migration, as well as regulates the secretion of other growth factors [84].

A widely recognized strategy for enhancing the regenerative potential of biomaterials entails the incorporation of bioactive substances that promote the release of GFs from cells involved in tissue regeneration. Notably, this approach highlights the use of Au NPs as a critical component. It has been demonstrated that integrating phytochemically stabilized Au NPs into hydrocolloid membranes (HCM) induced a

transient elevation in collagen synthesis within the ECM, which normalized by the fifteenth day following acute skin injury [85]. This effect holds significant importance, as it not only reduces the likelihood of hypertrophic scar formation but also concurrently stimulates the secretion of vascular endothelial growth factor (VEGF), a key regulator of angiogenesis. The proangiogenic properties of Au NPs, along with their ability to accelerate wound healing both *in vitro* and *in vivo*, were substantiated by a study conducted on rat models utilizing poly(lactic-co-glycolic acid) (PLGA) matrices encapsulating Au NPs in conjunction with polydopamine (PDA) [86]. Au NPs have been shown to facilitate wound closure by enhancing the expression levels of the NANOG transcription factor and the transmembrane adhesion protein CD34 [87]. Au NPs, coated with collagen I to enhance internalization by human dermal fibroblasts, promoted *in vitro* wound closure, significantly increasing the synthesis of VEGF and bFGF, thereby stimulating cellular proliferation [88]. Furthermore, Au NPs integrated within diverse matrix compositions exhibit not only proregenerative effects on cutaneous tissues, evidenced by the promotion of neo-vascularization and the formation of functional tissue, but also possess significant antibacterial properties, particularly when suspended in hydrogel [89] or electrospun within a PCL and gelatin blend [90].

5. Conclusions

The results substantiate the biofunctional efficacy of the biocompatible PLLA+GO-Au cell scaffold in the context of skin cell interactions, specifically keratinocytes and fibroblasts, as well as within a reconstructed epidermal environment. The PLLA+GO-Au scaffold demonstrates a significant enhancement in the adhesion of keratinocytes and fibroblasts, likely due to induced alterations in cytoskeletal architecture and upregulation of CAMs. This includes integrins, which facilitate cell-substrate adhesion, alongside E-cadherins, β -catenin and FAK, which are associated with cell-cell adhesion dynamics. Furthermore, the PLLA+GO-Au scaffold is capable of modulating epidermis tissue growth and regenerative processes through its ability to control the release of growth factors. An increase in the secretion levels of AREG, bFGF, EGF and EGF R was observed in keratinocytes. In contrast, fibroblasts exhibited only minor fluctuations in growth factor secretion profile, maintaining levels that were comparable to the control. This observation suggests that the PLLA nanostructured with GO-Au may modulate the release of growth factors across different cell populations, potentially mitigating adverse effects associated with hypertrophic growth. The biological effects observed in this study can be ascribed to the synergistic interactions arising from multiple factors: the unique mechanical properties of the PLLA+GO-Au composite scaffold and the nanoporous architecture of the PLLA fibers. Thus, the strategically designed PLLA+GO-Au embedded with cells, may represent an innovative therapeutic approach to facilitate precise processes in skin tissue growth and reconstruction.

CRedit authorship contribution statement

Michał Pruchniewski: Writing – review & editing, Writing – original draft, Visualization, Validation, Resources, Project administration, Methodology, Investigation, Funding acquisition, Formal analysis, Conceptualization. **Barbara Strojny-Cieślak:** Writing – review & editing, Supervision, Resources, Project administration, Funding acquisition, Formal analysis, Conceptualization. **Paweł Nakielski:** Writing – review & editing, Resources, Methodology, Investigation, Formal analysis. **Katarzyna Zawadzka:** Writing – original draft, Investigation. **Kaja Urbńska:** Investigation. **Daniel Rybak:** Investigation. **Anna Zakrzewska:** Investigation. **Marta Grodzik:** Resources. **Ewa Sawosz:** Supervision, Funding acquisition.

Declaration of competing interest

The authors declare that they have no known competing financial interests or personal relationships that could have appeared to influence the work reported in this paper.

Acknowledgment

The research was supported by the National Science Center (NCN) of Poland, Grant Preludium (grant number 2023/49/N/NZ4/02186). The publication was financed by Science development fund of the Warsaw University of Life Sciences – SGGW. The manuscript is part of the PhD thesis of Michał Pruchniewski.

Data availability

Data will be made available on request.

References

- [1] F. Akter, Principles of Tissue Engineering, Tissue Engineering Made Easy (2016) 3–16, <https://doi.org/10.1016/B978-0-12-805361-4.00002-3>.
- [2] F.J. O'Brien, Biomaterials & scaffolds for tissue engineering, Mater. Today 14 (2011) 88–95, [https://doi.org/10.1016/S1369-7021\(11\)70058-X](https://doi.org/10.1016/S1369-7021(11)70058-X).
- [3] B.P. Chan, K.W. Leong, Scaffolding in tissue engineering: general approaches and tissue-specific considerations, Eur. Spine J. 17 (2008) 467, <https://doi.org/10.1007/S00586-008-0745-3>.
- [4] S.A. Eming, P. Martin, M. Tomic-Canic, Wound repair and regeneration: Mechanisms, signaling, and translation, Sci Transl Med 6 (2014) 265sr6, <https://doi.org/10.1126/SCITRANSLMED.3009337>.
- [5] P. Lu, K. Takai, V.M. Weaver, Z. Werb, Extracellular Matrix Degradation and Remodeling in Development and Disease, Cold Spring Harb. Perspect. Biol. 3 (2011), <https://doi.org/10.1101/CSHPERSPECT.A005058>.
- [6] M.J. Jones, M.C. Jones, Cell cycle control by cell-matrix interactions, Curr. Opin. Cell Biol. 86 (2024) 102288, <https://doi.org/10.1016/J.CEB.2023.102288>.
- [7] F. Gattazzo, A. Urciuolo, P. Bonaldo, Extracellular matrix: A dynamic microenvironment for stem cell niche, Biochimica et Biophysica Acta (BBA) - General Subjects 1840 (2014) 2506–2519, <https://doi.org/10.1016/J.BBAGEN.2014.01.010>.
- [8] Z.C. Wang, W.Y. Zhao, Y. Cao, Y.Q. Liu, Q. Sun, P. Shi, J.Q. Cai, X.Z. Shen, W. Q. Tan, The Roles of Inflammation in Keloid and Hypertrophic Scars, Front. Immunol. 11 (2020) 603187, <https://doi.org/10.3389/FIMMU.2020.603187/BIBTEX>.
- [9] N.J. Schaub, T. Britton, R. Rajachar, R.J. Gilbert, Engineered nanotopography on electrospun PLLA microfibers modifies RAW 264.7 cell response, ACS Appl Mater Interfaces 5 (2013) 10173–10184. doi: 10.1021/AM402827G/SUPPL_FILE/AM402827G_SI_001.PDF.
- [10] Q. Zhou, J. Xie, M. Bao, H. Yuan, Z. Ye, X. Lou, Y. Zhang, Engineering aligned electrospun PLLA microfibers with nano-porous surface nanotopography for modulating the responses of vascular smooth muscle cells, J. Mater. Chem. B 3 (2015) 4439–4450, <https://doi.org/10.1039/C5TB00051C>.
- [11] J. Luo, M. Walker, Y. Xiao, H. Donnelly, M.J. Dalby, M. Salmeron-Sanchez, The influence of nanotopography on cell behaviour through interactions with the extracellular matrix – A review, Bioact. Mater. 15 (2022) 145, <https://doi.org/10.1016/J.BIOACTMAT.2021.11.024>.
- [12] S.D. Yoon, Y.S. Kwon, K.S. Lee, Biodegradation and Biocompatibility of Poly L-lactic Acid Implantable Mesh, Int. Neurolog. J. 21 (2017) S48, <https://doi.org/10.5213/INJ.1734882.441>.
- [13] D. Pappalardo, T. Mathisen, A. Finne-Wistrand, Biocompatibility of Resorbable Polymers: A Historical Perspective and Framework for the Future, Biomacromolecules 20 (2019) 1465–1477, https://doi.org/10.1021/ACS.BIOMAC.9B00159/ASSET/IMAGES/LARGE/BM-2019-00159C_0006.JPEG.
- [14] J.R.G. Carvalho, G. Conde, M.L. Antonioli, P.P. Dias, R.O. Vasconcelos, S.R. Taboga, P.A. Canola, M.A. Chinellato, G.T. Pereira, G.C. Ferraz, Biocompatibility and biodegradation of poly(lactic acid) (PLA) and an immiscible PLA/poly(ϵ -caprolactone) (PCL) blend compatibilized by poly(ϵ -caprolactone-*b*-tetrahydrofuran) implanted in horses, Polymer Journal 2020 52:6 52 (2020) 629–643. doi: 10.1038/s41428-020-0308-y.
- [15] M. Schroeffer, F. Junghans, D. Voigt, M. Meyer, A. Breier, G. Schulze-Tanzil, I. Prade, Gas-Phase Fluorination on PLA Improves Cell Adhesion and Spreading, ACS Omega 5 (2020) 5498–5507, https://doi.org/10.1021/ACSOMEGA.0C00126/ASSET/IMAGES/MEDIUM/AOOC00126_M001.GIF.
- [16] G. Martelli, N. Bloise, A. Merlettoni, G. Bruni, L. Visai, M.L. Focarete, D. Giacomini, Combining Biologically Active β -Lactams Integrin Agonists with Poly(l-lactic acid) Nanofibers: Enhancement of Human Mesenchymal Stem Cell Adhesion, Biomacromolecules 21 (2020) 1157–1170, https://doi.org/10.1021/ACS.BIOMAC.9B01550/ASSET/IMAGES/LARGE/BM9B01550_0006.JPEG.
- [17] D. Solarz, T. Witko, R. Karcz, I. Malagurski, M. Ponjavic, S. Levic, A. Nestic, M. Guzik, S. Savic, J. Nikodinovic-Runic, Biological and physiochemical studies of electrospun polylactid/polyhydroxyoctanoate PLA/P(3HO) scaffolds for tissue

- engineering applications, *RSC Adv.* 13 (2023) 24112–24128, <https://doi.org/10.1039/D3RA03021K>.
- [18] Y. Dong, Y. Zhang, H. Yu, L. Zhou, Y. Zhang, H. Wang, Z. Hu, S. Luo, Poly-l-lactic acid microspheres delay aging of epidermal stem cells in rat skin, *Front. Immunol.* 15 (2024) 1394530, <https://doi.org/10.3389/FIMMU.2024.1394530/BIBTEX>.
- [19] H. Shokry, U. Vanamo, O. Wiltschka, J. Niinimäki, M. Lerche, K. Levon, M. Linden, C. Sahlgren, Mesoporous silica particle-PLA–PANI hybrid scaffolds for cell-directed intracellular drug delivery and tissue vascularization, *Nanoscale* 7 (2015) 14434–14443, <https://doi.org/10.1039/C5NR03983E>.
- [20] H.H. Yoon, S.H. Bhang, T. Kim, T. Yu, T. Hyeon, B.S. Kim, Dual Roles of Graphene Oxide in Chondrogenic Differentiation of Adult Stem Cells: Cell-Adhesion Substrate and Growth Factor-Delivery Carrier, *Adv. Funct. Mater.* 24 (2014) 6455–6464, <https://doi.org/10.1002/ADFM.201400793>.
- [21] J.T. Jeong, M.K. Choi, Y. Sim, J.T. Lim, G.S. Kim, M.J. Seong, J.H. Hyung, K.S. Kim, A. Umar, S.K. Lee, Effect of graphene oxide ratio on the cell adhesion and growth behavior on a graphene oxide-coated silicon substrate, *Scientific Reports* 2016 6:1 6 (2016) 1–10. doi: 10.1038/srep33835.
- [22] M. Pruchniewski, E. Sawosz, M. Sosnowska-Lawnicka, A. Ostrowska, M. Łojkowski, P. Koczoń, P. Nakielski, M. Kutwin, S. Jaworski, B. Strojny-Cieślak, Nanostructured graphene oxide enriched with metallic nanoparticles as a biointerface to enhance cell adhesion through mechanosensory modifications, *Nanoscale* 15 (2023) 18639–18659, <https://doi.org/10.1016/J.COLSURFB.2010.06.019>.
- [23] B. Strojny-Cieślak, S. Jaworski, M. Wierzbicki, M. Pruchniewski, M. Sosnowska-Lawnicka, J. Szczepaniak, A. Lange, P. Koczoń, M. Zielińska-Górska, E. S. Chwalibóg, The cytocompatibility of graphene oxide as a platform to enhance the effectiveness and safety of silver nanoparticles through in vitro studies, *Environ. Sci. Pollut. Res.* (2023) 1–22, <https://doi.org/10.1007/S11356-023-30151-1/FIGURES/17>.
- [24] S. Lu, D. Xia, G. Huang, H. Jing, Y. Wang, H. Gu, Concentration effect of gold nanoparticles on proliferation of keratinocytes, *Colloids Surf. B Biointerfaces* 81 (2010) 406–411, <https://doi.org/10.1016/J.COLSURFB.2010.06.019>.
- [25] V.V. Sumbayev, I.M. Yasinska, C.P. Garcia, D. Gilliland, G.S. Lall, B.F. Gibbs, D. R. Bonsall, L. Varani, F. Rossi, L. Calzolari, Gold Nanoparticles Downregulate Interleukin-1 β -Induced Pro-Inflammatory Responses, *Small* 9 (2013) 472–477, <https://doi.org/10.1002/SMLL.201201528>.
- [26] H. Rizwan, J. Mohanta, S. Si, A. Pal, Gold nanoparticles reduce high glucose-induced oxidative-nitrosative stress regulated inflammation and apoptosis via tuberlin-mTOR/NF- κ B pathways in macrophages, *Int. J. Nanomed.* 12 (2017) 5841–5862, <https://doi.org/10.2147/IJN.S141839>.
- [27] K.C. Chou, J.H. Cherng, K.L. Ou, Y.W. Wang, Gold nanoclusters on a silk fibroin scaffold accelerate fibroblast proliferation and improve burn recovery in a mouse burn model, *Mater. Des.* 244 (2024) 113221, <https://doi.org/10.1016/J.MATDES.2024.113221>.
- [28] C. Huang, J. Dong, Y. Zhang, S. Chai, X. Wang, S. Kang, D. Yu, P. Wang, Q. Jiang, Gold Nanoparticles-Loaded Polyvinylpyrrolidone/Ethylcellulose Coaxial Electrospun Nanofibers with Enhanced Osteogenic Capability for Bone Tissue Regeneration, *Mater. Des.* 212 (2021) 110240, <https://doi.org/10.1016/J.MATDES.2021.110240>.
- [29] W.K. Ko, H. Nah, S.J. Kim, G.H. Han, D. Lee, J.S. Lee, D.N. Heo, D. Lee, S.J. Lee, M. Heo, S.H. Sheen, I.K. Kwon, S. Sohn, The effects of aligned poly(lactic-co-glycolic acid) nanofibrous mat containing gold nanoparticles after planting onto an injured spinal cord, *Mater. Des.* 232 (2023) 112181, <https://doi.org/10.1016/J.MATDES.2023.112181>.
- [30] G. Wang, G. Qian, J. Zan, F. Qi, Z. Zhao, W. Yang, S. Peng, C. Shuai, A co-dispersion nanosystem of graphene oxide @silicon-doped hydroxyapatite to improve scaffold properties, *Mater. Des.* 199 (2021) 109399, <https://doi.org/10.1016/J.MATDES.2020.109399>.
- [31] X. Ou, L. Guan, W. Guo, X. Zhang, S. Wu, D. Guo, R. Li, A.V. Zvyagin, Q. Lin, W. Qu, Graphene oxide-based injectable conductive hydrogel dressing with immunomodulatory for chronic infected diabetic wounds, *Mater. Des.* 224 (2022) 111284, <https://doi.org/10.1016/J.MATDES.2022.111284>.
- [32] S. Saravanan, N. Sareen, E. Abu-El-Rub, H. Ashour, G.L. Sequiera, H.I. Ammar, V. Gopinath, A.A. Shamaa, S.S.E. Sayed, M. Moudgil, J. Vaidvelu, S. Dhingra, Graphene Oxide-Gold Nanosheets Containing Chitosan Scaffold Improves Ventricular Contractility and Function After Implantation into Infarcted Heart, *Scientific Reports* 2018 8:1 8 (2018) 1–13. doi: 10.1038/s41598-018-33144-0.
- [33] S.Z. Nergiz, N. Gandra, S. Tadepalli, S. Singamaneni, Multifunctional hybrid nanopatches of graphene oxide and gold nanostars for ultraefficient photothermal cancer therapy, *ACS Appl. Mater. Interfaces* 6 (2014) 16395–16402, https://doi.org/10.1021/AM504795D/SUPPL_FILE/AM504795D_SI_001.PDF.
- [34] S. Kang, J. Lee, S. Ryu, Y. Kwon, K.H. Kim, D.H. Jeong, S.R. Paik, B.S. Kim, Gold Nanoparticle/Graphene Oxide Hybrid Sheets Attached on Mesenchymal Stem Cells for Effective Photothermal Cancer Therapy, *Chem. Mater.* 29 (2017) 3461–3476, https://doi.org/10.1021/ACS.CHEMMATER.6B05164/SUPPL_FILE/CM6B05164_SI_001.PDF.
- [35] D. Duc, P.R. Stoddart, S.L. McArthur, R.M.I. Kapsa, A.F. Quigley, M. Boyd-Moss, S. E. Moulton, Fabrication of a Biocompatible Liquid Crystal Graphene Oxide–Gold Nanorods Electro- and Photoactive Interface for Cell Stimulation, *Adv. Healthc. Mater.* 8 (2019) 1801321, <https://doi.org/10.1002/ADHM.201801321>.
- [36] M. Li, W. Deng, J. Zhang, W. Zheng, T. Yu, Q. Zhou, Aligned Electrospun PLLA/Graphene Microfibers with Nanotopographical Surface Modulate the Mitochondrial Responses of Vascular Smooth Muscle Cells, *Adv. Mater. Interfaces* 8 (2021) 2100229, <https://doi.org/10.1002/ADMI.202100229>.
- [37] P. Jain, R. Rimal, M. Möller, S. Singh, Topographical influence of electrospun basement membrane mimics on formation of cellular monolayer, *Scientific Reports* 2023 13:1 13 (2023) 1–14. doi: 10.1038/s41598-023-34934-x.
- [38] R. Ramírez-Jiménez, M. Franco, E. Rodrigo, R. Sainz, R. Ferritto, A.M. Lamsabhi, J. L. Aceña, M.B. Cid, Unexpected reactivity of graphene oxide with DBU and DMF, *J Mater Chem A Mater* 6 (2018) 12637–12646, <https://doi.org/10.1039/C8TA03529F>.
- [39] M.I. Sujan, S.D. Sarkar, C.K. Roy, M. Ferdous, A. Goswami, M.A. Gafur, M.S. Azam, Graphene oxide crosslinker for the enhancement of mechanical properties of polylactic acid, *J. Polym. Sci.* 59 (2021) 1043–1054, <https://doi.org/10.1002/POL.20210029>.
- [40] W. Li, Z. Xu, L. Chen, M. Shan, X. Tian, C. Yang, H. Lv, X. Qian, A facile method to produce graphene oxide-g-poly(L-lactic acid) as an promising reinforcement for PLLA nanocomposites, *Chem. Eng. J.* 237 (2014) 291–299, <https://doi.org/10.1016/J.CEJ.2013.10.034>.
- [41] G. Gedler, M. Antunes, V. Realinho, J.I. Velasco, Thermal stability of polycarbonate-graphene nanocomposite foams, *Polym. Degrad. Stab.* 97 (2012) 1297–1304, <https://doi.org/10.1016/J.POLYMEDEGRADSTAB.2012.05.027>.
- [42] T. Gu, D. Xiang Sun, X. Dong Qi, J. Hui Yang, Y. Zhou Lei, Y. Wang, Heat resistant and thermally conductive polylactide composites achieved by stereocomplex crystallite tailored carbon nanofiber network, *Chem. Eng. J.* 418 (2021) 129287, <https://doi.org/10.1016/J.CEJ.2021.129287>.
- [43] Y. Li, Z. Wen, Y. Luan, D. Sun, J. Yang, Strengthening and toughening design of graphene oxide based artificial nacre composites regulated by dimensional hierarchy of ternary structure, *Compos. A Appl. Sci. Manuf.* 179 (2024) 108015, <https://doi.org/10.1016/J.COMPOSITESA.2024.108015>.
- [44] B. Wang, Y. Li, G. Weng, Z. Jiang, P. Chen, Z. Wang, Q. Gu, Reduced graphene oxide enhances the crystallization and orientation of poly(ϵ -caprolactone), *Compos. Sci. Technol.* 96 (2014) 63–70, <https://doi.org/10.1016/J.COMPOSITECH.2014.03.012>.
- [45] M. Cano, U. Khan, T. Sainsbury, A. O'Neill, Z. Wang, I.T. McGovern, W.K. Maser, A. M. Benito, J.N. Coleman, Improving the mechanical properties of graphene oxide based materials by covalent attachment of polymer chains, *Carbon N Y* 52 (2013) 363–371, <https://doi.org/10.1016/J.CARBON.2012.09.046>.
- [46] A. Ammar, A.M. Al-Enizi, M.A.A. AlMaadeed, A. Karim, Influence of graphene oxide on mechanical, morphological, barrier, and electrical properties of polymer membranes, *Arab. J. Chem.* 9 (2016) 274–286, <https://doi.org/10.1016/J.ARABJC.2015.07.006>.
- [47] O.C. Compton, S.W. Cranford, K.W. Putz, Z. An, L.C. Brinson, M.J. Buehler, S. T. Nguyen, Tuning the mechanical properties of graphene oxide paper and its associated polymer nanocomposites by controlling cooperative intersheet hydrogen bonding, *ACS Nano* 6 (2012) 2008–2019, https://doi.org/10.1021/NN202928W/SUPPL_FILE/NN202928W_SI_001.PDF.
- [48] X. Zhou, D. Li, S. Wan, Q. Cheng, B. Ji, In silicon testing of the mechanical properties of graphene oxide-silk nanocomposites, *Acta Mech.* 230 (2019) 1413–1425, <https://doi.org/10.1007/S00707-017-2017-Y>.
- [49] D. Galpaya, M. Wang, G. George, N. Motta, E. Waclawik, C. Yan, Preparation of graphene oxide/epoxy nanocomposites with significantly improved mechanical properties, *J. Appl. Phys.* 116 (2014), <https://doi.org/10.1063/1.4892089>.
- [50] F. Jiang, Y. Shan, J. Tian, L. Xu, C. Li, F. Yu, X. Cui, C. Wang, Z. Li, K. Ren, Poly(L-Lactic Acid) Nanofiber-Based Multilayer Film for the Electrical Stimulation of Nerve Cells, *Adv. Mater. Interfaces* 10 (2023) 2202474, <https://doi.org/10.1002/ADMI.202202474>.
- [51] M. Polak, K. Berniak, P.K. Szewczyk, J.E. Karbowiczek, M.M. Marzec, U. Stachewicz, PLLA scaffolds with controlled surface potential and piezoelectricity for enhancing cell adhesion in tissue engineering, *Appl. Surf. Sci.* 621 (2023) 156835, <https://doi.org/10.1016/J.APSUSC.2023.156835>.
- [52] A. Ravindran Girija, V. Palaninathan, X. Strudwick, S. Balasubramanian, S. Dasappan Nair, A.J. Cowin, Collagen-functionalized electrospun smooth and porous polymeric scaffolds for the development of human skin-equivalent, *RSC Adv.* 10 (2020) 26594, <https://doi.org/10.1039/D0RA04648E>.
- [53] A. Ferrández-Montero, M. Lieblich, J.L. González-Carrasco, R. Benavente, V. Lorenzo, R. Detsch, A.R. Boccaccini, B. Ferrari, Development of biocompatible and fully bioabsorbable PLA/Mg films for tissue regeneration applications, *Acta Biomater.* 98 (2019) 114–124, <https://doi.org/10.1016/J.ACTBIO.2019.05.026>.
- [54] W. Chen H. Zhao Y. Li Mitochondrial dynamics in health and disease: mechanisms and potential targets, *Signal Transduction and Targeted Therapy* 2023 10.1038/s41392-023-01547-9 1 25.
- [55] M.F. Abazari, N. Nasiri, F. Nejati, M. Kohandani, N. Hajati-Birgani, S. Sadeghi, P. Piri, F. Soleimanifar, M. Rezaei-Tavirani, V. Mansouri, Acceleration of osteogenic differentiation by sustained release of BMP2 in PLLA/graphene oxide nanofibrous scaffold, *Polym. Adv. Technol.* 32 (2021) 272–281, <https://doi.org/10.1002/PAT.5083>.
- [56] B. Li, F. Xiong, B. Yao, Q. Du, J. Cao, J. Qu, W. Feng, H. Yuan, Preparation and characterization of antibacterial dopamine-functionalized reduced graphene oxide/PLLA composite nanofibers, *RSC Adv.* 10 (2020) 18614–18623, <https://doi.org/10.1039/D0RA03224G>.
- [57] C. Shuai, Y. Li, W. Yang, L. Yu, Y. Yang, S. Peng, P. Feng, Graphene Oxide Induces Ester Bonds Hydrolysis of Poly-l-lactic Acid Scaffold to Accelerate Degradation, *Int J Bioprint* 6 (2020) 91–104, <https://doi.org/10.18063/IJB.V6I1.249>.
- [58] A. Kalra, A. Lowe, An Overview of Factors Affecting the Skins Youngs Modulus, *J Aging Sci* 4 (2016), <https://doi.org/10.4172/2329-8847.1000156>.
- [59] C. Jaquemoud, K. Bruyere-Garnier, M. Coret, Methodology to determine failure characteristics of planar soft tissues using a dynamic tensile test, *J. Biomech.* 40 (2007) 468–475, <https://doi.org/10.1016/J.JBIOMECH.2005.12.010>.
- [60] J. Van Kullenburg, M.A. Masen, E. Van Der Heide, Contact modelling of human skin: What value to use for the modulus of elasticity?, <http://dx.doi.org/10.1177/1350650112463307> 227 (2012) 349–361. doi: 10.1177/1350650112463307.

- [61] E. Mazza, A.E. Ehret, Mechanical biocompatibility of highly deformable biomedical materials, *J. Mech. Behav. Biomed. Mater.* 48 (2015) 100–124, <https://doi.org/10.1016/j.jmbm.2015.03.023>.
- [62] V. Panzetta, D. Guarnieri, A. Paciello, F. Della Sala, O. Muscetti, L. Raiola, P. Netti, S. Fusco, ECM Mechano-Sensing Regulates Cytoskeleton Assembly and Receptor-Mediated Endocytosis of Nanoparticles, *ACS Biomater Sci Eng* 3 (2017) 1586–1594. doi: 10.1021/ACSBOMATERIALS.7B00018/SUPPL_FILE/AB7B00018_SI_001.PDF.
- [63] J. Nam, J. Johnson, J.J. Lannutti, S. Agarwal, Modulation of embryonic mesenchymal progenitor cell differentiation via control over pure mechanical modulus in electrospun nanofibers, *Acta Biomater.* 7 (2011) 1516–1524, <https://doi.org/10.1016/j.actbio.2010.11.022>.
- [64] V. Lulevich, H.-Y. Yang, R. Rivkah Isseroff, G.-Y. Liu, Single cell mechanics of keratinocyte cells, *Ultramicroscopy* 110 (2010) 1435–1442, <https://doi.org/10.1016/j.ultramic.2010.07.009>.
- [65] S. Nedjari, F. Awaja, G. Altankov, Three Dimensional Honeycomb Patterned Fibrinogen Based Nanofibers Induce Substantial Osteogenic Response of Mesenchymal Stem Cells, *Scientific Reports* 2017 7:1 7 (2017) 1–11. doi: 10.1038/s41598-017-15956-8.
- [66] S.Y. Chew, R. Mi, A. Hoke, K.W. Leong, The effect of the alignment of electrospun fibrous scaffolds on Schwann cell maturation, *Biomaterials* 29 (2008) 653–661, <https://doi.org/10.1016/j.biomaterials.2007.10.025>.
- [67] X. Pang, X. He, Z. Qiu, H. Zhang, R. Xie, Z. Liu, Y. Gu, N. Zhao, Q. Xiang, Y. Cui, Targeting integrin pathways: mechanisms and advances in therapy, *Signal Transduction and Targeted Therapy* 2022 8:1 8 (2023) 1–42. doi: 10.1038/s41392-022-01259-6.
- [68] X. Tian, Z. Liu, B. Niu, J. Zhang, T.K. Tan, S.R. Lee, Y. Zhao, D.C.H. Harris, G. Zheng, E-Cadherin/ β -Catenin Complex and the Epithelial Barrier, *J. Biomed. Biotechnol.* 2011 (2011), <https://doi.org/10.1155/2011/567305>.
- [69] X. Tan, Y. Yan, B. Song, S. Zhu, Q. Mei, K. Wu, Focal adhesion kinase: from biological functions to therapeutic strategies, *Exp. Hematol. Oncol.* 12 (2023) 1–19, <https://doi.org/10.1186/s40164-023-00466-7/TABLES/3>.
- [70] Z. Qiu, X. Lin, L. Zou, W. Fu, H. Lv, Effect of graphene oxide/ poly-L-lactic acid composite scaffold on the biological properties of human dental pulp stem cells, *BMC Oral Health* 24 (2024), <https://doi.org/10.1186/s12903-024-04197-7>.
- [71] K. Zhang, H. Zheng, S. Liang, C. Gao, Aligned PLLA nanofibrous scaffolds coated with graphene oxide for promoting neural cell growth, *Acta Biomater.* 37 (2016) 131–142, <https://doi.org/10.1016/j.actbio.2016.04.008>.
- [72] S. Pandit, M. De, Interaction of amino acids and graphene oxide: Trends in thermodynamic properties, *J. Phys. Chem. C* 121 (2017) 600–608, https://doi.org/10.1021/ACS.jpcc.6b11571/SUPPL_FILE/JP6B11571_SI_001.PDF.
- [73] L. Wu, L. Zeng, X. Jiang, Revealing the nature of interaction between graphene oxide and lipid membrane by surface-enhanced infrared absorption spectroscopy, *J. Am. Chem. Soc.* 137 (2015) 10052–10055, https://doi.org/10.1021/JACS.5B03803/SUPPL_FILE/JA5B03803_SI_001.PDF.
- [74] J.-B.; Park, D.-B.; Lee, J.-H.; Yang, S.-J.; Lee, J.-E.; Park, J.-K.; Huh, J.-S.; Lim, J.-B. Park, D.-B. Park, J.-H. Lee, S.-J. Yang, J.-E. Lee, J.-K. Park, J.-S. Huh, J.-O. Lim, Application of Graphene Oxide as a Biomaterial for the Development of Large-Area Cell Culture Vessels, *Applied Sciences* 2022, Vol. 12, Page 11599 12 (2022) 11599. doi: 10.3390/AP122211599.
- [75] M. Wierzbicki, A. Hotowy, M. Kutwin, S. Jaworski, J. Bałaban, M. Sosnowska, B. Wójcik, A. Wędzińska, A. Chwalibog, E. Sawosz, Graphene Oxide Scaffold Stimulates Differentiation and Proangiogenic Activities of Myogenic Progenitor Cells, *International Journal of Molecular Sciences* 2020, Vol. 21, Page 4173 21 (2020) 4173. doi: 10.3390/IJMS21114173.
- [76] Y. Sun, K. Zhang, R. Deng, X. Ren, C. Wu, J. Li, Tunable stiffness of graphene oxide/polyacrylamide composite scaffolds regulates cytoskeleton assembly, *Chem. Sci.* 9 (2018) 6516–6522, <https://doi.org/10.1039/C8SC02100G>.
- [77] E. Ngandu Mpoyi, M. Cantini, P.M. Reynolds, N. Gadegaard, M.J. Dalby, M. Salmerón-Sánchez, Protein Adsorption as a Key Mediator in the Nanotopographical Control of Cell Behavior, *ACS Nano* 10 (2016) 6638–6647, <https://doi.org/10.1021/ACS.NANO.6B01649/ASSET/IMAGES/LARGE/NN-2016-011649R.0008.JPEG>.
- [78] E.K.F. Yim, E.M. Darling, K. Kulangara, F. Guilak, K.W. Leong, Nanotopography-induced changes in focal adhesions, cytoskeletal organization, and mechanical properties of human mesenchymal stem cells, *Biomaterials* 31 (2010) 1299–1306, <https://doi.org/10.1016/j.biomaterials.2009.10.037>.
- [79] H. Zheng, Y. Tian, Q. Gao, Y. Yu, X. Xia, Z. Feng, F. Dong, X. Wu, L. Sui, Hierarchical Micro-Nano Topography Promotes Cell Adhesion and Osteogenic Differentiation via Integrin α 2-P13K-AKT Signaling Axis, *Front. Bioeng. Biotechnol.* 8 (2020) 544372, <https://doi.org/10.3389/fbioe.2020.00463/BIBTEX>.
- [80] L. Jing, X. Wang, B. Leng, N. Zhan, H. Liu, S. Wang, Y. Lu, J. Sun, D. Huang, Engineered Nanotopography on the Microfibers of 3D-Printed PCL Scaffolds to Modulate Cellular Responses and Establish an in Vitro Tumor Model, *ACS Appl. Bio Mater.* 4 (2021) 1381–1394, https://doi.org/10.1021/ACSABM.0C01243/SUPPL_FILE/MT0C01243_SI_001.PDF.
- [81] P.M. Comoglio, C. Boccaccio, L. Trusolino, Interactions between growth factor receptors and adhesion molecules: breaking the rules, *Curr. Opin. Cell Biol.* 15 (2003) 565–571, [https://doi.org/10.1016/S0955-0674\(03\)00096-6](https://doi.org/10.1016/S0955-0674(03)00096-6).
- [82] J. Lu, K. Squillace, M.R. Pittelkow, Identification of the Effect of Amphiregulin on Keratinocytes and T Cells in Psoriasis, *DOI: 10.1177/247553031016a00201* 16a (2018) 4–8. doi: 10.1177/247553031016a00201.
- [83] R. Zare, H. Abdolsamadi, S.S. Asl, S. Radi, H. Bahrami, S. Jamshidi, The bFGF Can Improve Angiogenesis in Oral Mucosa and Accelerate Wound Healing, *Rep Biochem Mol Biol* 11 (2023) 547, <https://doi.org/10.52547/RBMB.11.4.547>.
- [84] A. Yu, Y. Matsuda, A. Takeda, E. Uchinuma, Y. Kuroyanagi, Effect of EGF and bFGF on fibroblast proliferation and angiogenic cytokine production from cultured dermal substitutes, *J. Biomater. Sci. Polym. Ed.* 23 (2012) 1315–1324, <https://doi.org/10.1163/092050611X580463>.
- [85] J.E. Kim, J. Lee, M. Jang, M.H. Kwak, J. Go, E.K. Kho, S.H. Song, J.E. Sung, J. Lee, D.Y. Hwang, Accelerated healing of cutaneous wounds using phytochemically stabilized gold nanoparticle deposited hydrocolloid membranes, *Biomater. Sci.* 3 (2015) 509–519, <https://doi.org/10.1039/C4BM00390J>.
- [86] Y. Dong, Z. Wang, J. Wang, X. Sun, X. Yang, G. Liu, Mussel-inspired electroactive, antibacterial and antioxidative composite membranes with incorporation of gold nanoparticles and antibacterial peptides for enhancing skin wound healing, *J. Biol. Eng.* 18 (2024) 1–19, <https://doi.org/10.1186/S13036-023-00402-3/FIGURES/12>.
- [87] Z. Batool, G. Muhammad, M.M. Iqbal, M.S. Aslam, M.A. Raza, N. Sajjad, M. Abdullah, N. Akhtar, A. Syed, A.M. Elgorban, S.S. Al-Rejaie, Z. Shafiq, Hydrogel assisted synthesis of gold nanoparticles with enhanced microbicidal and in vivo wound healing potential, *Scientific Reports* 2022 12:1 12 (2022) 1–10. doi: 10.1038/s41598-022-10495-3.
- [88] S. Poomrattanagoon, D. Pissuwan, Gold nanoparticles coated with collagen-I and their wound healing activity in human skin fibroblast cells, *Heliyon* 10 (2024), <https://doi.org/10.1016/j.heliyon.2024.e33302>.
- [89] W. Chen, R. Chu, H. Li, T. Hua, H. Chen, R. Li, D. Zhou, S. Cao, S. Ye, H. Li, A novel wound dressing based on a gold nanoparticle self-assembled hydrogel to promote wound healing, *Mater. Adv.* 4 (2023) 2918–2925, <https://doi.org/10.1039/D3MA00130J>.
- [90] X. Yang, J. Yang, L. Wang, B. Ran, Y. Jia, L. Zhang, G. Yang, H. Shao, X. Jiang, Pharmaceutical Intermediate-Modified Gold Nanoparticles: Against Multidrug-Resistant Bacteria and Wound-Healing Application via an Electrospun Scaffold, *ACS Nano* 11 (2017) 5737–5745, https://doi.org/10.1021/ACS.NANO.7B01240/SUPPL_FILE/NN7B01240_SI_001.PDF.